

An Extremely Young Protostellar Core, MMS 1/ OMC-3: Episodic Mass Ejection History Traced by the Micro SiO Jet

SATOKO TAKAHASHI ^{1,2} MASAHIRO N. MACHIDA ³ MITSUKI OMURA ⁴ DOUG JOHNSTONE ^{5,6} KAZUYA SAIGO ⁷
NAOTO HARADA ⁴ KOHJI TOMISAKA ¹ PAUL T. P. HO ^{8,9} LUIS A. ZAPATA ¹⁰ STEVE MAIRS ^{9,5}
GREGORY J. HERCZEG ^{11,12} KOTOMI TANIGUCHI ¹ YUHUA LIU ⁴ AND ASAKO SATO ⁴

¹National Astronomical Observatory of Japan, 2-21-1 Osawa, Mitaka, Tokyo 181-8588, Japan; satoko.takahashi@nao.ac.jp

²Astronomical Science Program, The Graduate University for Advanced Studies, SOKENDAI, 2-21-1 Osawa, Mitaka, Tokyo 181-8588, Japan

³Department of Earth and Planetary Sciences, Faculty of Science, Kyushu University, 744 Motooka, Nishi-ku, Fukuoka 819-0395, Japan

⁴Department of Earth and Planetary Sciences, Graduate School of Science, Kyushu University, 744 Motooka, Nishi-ku, Fukuoka 819-0395, Japan

⁵NRC Herzberg Astronomy and Astrophysics, 5071 West Saanich Rd, Victoria, BC, V9E 2E7, Canada

⁶Department of Physics and Astronomy, University of Victoria, Victoria, BC, V8P 5C2, Canada

⁷Department of Physics and Astronomy, Graduate School of Science and Engineering, Kagoshima University, 1-21-35 Korimoto, Kagoshima, Kagoshima 890-0065, Japan

⁸Institute of Astronomy and Astrophysics, Academia Sinica, 11F of Astronomy-Mathematics Building, AS/NTU No. 1, Sec. 4, Roosevelt Rd, Taipei 10617, Taiwan, R.O.C.

⁹East Asian Observatory, 660 N. A'ohoku Place, Hilo, HI 96720, USA

¹⁰Instituto de Radioastronomía y Astrofísica, Universidad Nacional Autónoma de México, PO Box 3-72, 58090 Morelia, Michoacán, México

¹¹Kavli Institute for Astronomy & Astrophysics, Peking University, Yiheyuan Lu 5, Haidian Qu, 100871 Beijing, People's Republic of China

¹²Department of Astronomy, Peking University, Yiheyuan 5, Haidian Qu, 100871 Beijing, People's Republic of China

ABSTRACT

We present ~ 0.2 arcsec (~ 80 au) resolution observations of the CO (2–1) and SiO (5–4) lines made with the Atacama large millimeter/submillimeter array toward an extremely young intermediate-mass protostellar source ($t_{\text{dyn}} < 1000$ years), MMS 1 located in the Orion Molecular Cloud-3 region. We have successfully imaged a very compact CO molecular outflow associated with MMS 1, having deprojected lobe sizes of ~ 18000 au (red-shifted lobe) and ~ 35000 au (blue-shifted lobe). We have also detected an extremely compact ($\lesssim 1000$ au) and collimated SiO protostellar jet within the CO outflow. The maximum deprojected jet speed is measured to be as high as 93 km s^{-1} . The SiO jet wiggles and displays a chain of knots. Our detection of the molecular outflow and jet is the first direct evidence that MMS 1 already hosts a protostar. The position-velocity diagram obtained from the SiO emission shows two distinct structures: (i) bow-shocks associated with the tips of the outflow, and (ii) a collimated jet, showing the jet velocities linearly increasing with the distance from the driving source. Comparisons between the observations and numerical simulations quantitatively share similarities such as multiple-mass ejection events within the jet and Hubble-like flow associated with each mass ejection event. Finally, while there is a weak flux decline seen in the $850 \mu\text{m}$ light curve obtained with JCMT/SCUBA 2 toward MMS 1, no dramatic flux change events are detected. This suggests that there has not been a clear burst event within the last 8 years.

Keywords: Star formation (1569) — Stellar jets (1807) — Stellar winds (1636), Protostars (1302) — Shocks (2086)

1. INTRODUCTION

Molecular outflows and jets are observed in low-to high-mass star-forming regions (Bachiller & Tafalla 1999; Arce et al. 2007; Bally 2016; Lee 2020 and references therein). They are spatially extended, hence a use-

ful tool to explore protostars when they are still deeply embedded within the core, and even when infrared counterparts are not detected at the peak position of the millimeter source (e.g., Takahashi et al. 2009; Takahashi & Ho 2012; Takahashi et al. 2019). Molecular outflows are ubiquitously observed toward protostars. Observationally, the molecular outflows are accompanied with a wide-opening angle cavity (or also called the outflow lobe), having the low- and intermediate-velocity ranges ($\lesssim 50 \text{ km s}^{-1}$). Protostellar jets are known as the extremely high velocity flow (a.k.a. EHV flow; Bachiller & Cernicharo 1990), which shows a collimated morphology with high velocity gas ($\gtrsim 50 \text{ km s}^{-1}$). Whereas the molecular outflows are ubiquitously observed, only seven EHV flows had been reported before ALMA. Furthermore, detection of the EHV jets was limited to bright Class 0 sources (Bachiller & Cernicharo 1990; Bachiller et al. 1991a,b; Bachiller 1996; Lebrón et al. 2006; Hirano et al. 2010; Gómez-Ruiz et al. 2013; Tafalla et al. 2017; Lee et al. 2017; Lee 2020). This field of study has grown with the improved sensitivity of ALMA, which enables us to image more EHV flows associated with both Class 0 and Class I protostellar stages (e.g., Matsushita et al. 2019; Jhan et al. 2022; Dutta et al. 2022, 2023).

In addition to sensitivity improvements, ALMA sub-arcsecond observations enable us to detect not only bright outflows and jets in the sky, but also fainter or compact (i.e., younger) ones (e.g., Zapata et al. 2015; Matsushita et al. 2019; Tokuda et al. 2020; Morii et al. 2021a). Searching for very compact molecular outflows and jets (\lesssim a few 1000 au) sheds light on the first stage of the star formation process such as formation of the first adiabatic cores (e.g., Larson 1969; Masunaga & Inutsuka 2000; Saigo & Tomisaka 2006; Maureira et al. 2020) and protostar formation immediately following the second collapse (e.g., Machida et al. 2007; Takahashi & Ho 2012; Takahashi et al. 2013b; Hirano & Liu 2014; Gerin et al. 2015).

The outflow and jet are driven by magnetocentrifugal and magnetic pressure gradient mechanisms (Blandford & Payne 1982; Uchida & Shibata 1985; Lynden-Bell 2003). ALMA's high angular resolution data can directly image the region near the launching point (Bjerkeli et al. 2016), allowing for a direct comparison with molecular outflows and jets produced by magnetohydrodynamics (MHD) models (e.g., Shu et al. 1994; Tomisaka 2002; Machida et al. 2007; Shang et al. 2023). With this in mind, we can push in the right direction to understand better the driving mechanisms of the jets and outflows.

Recent studies present evidence for time variable mass ejection and accretion phenomena more commonly (see review by Fischer et al. 2023). Periodically located knots (i.e., chain of knots) are detected by ALMA within some of the outflows and jets, using CO and SiO emission. These knots may be related to a periodic variation in the jet velocity and periodic change in the mass ejections (Plunkett et al. 2015; Matsushita et al. 2019; Jhan et al. 2022; Dutta et al. 2022, 2023). Dynamical timescales of each knot range from a few years to several thousands years. Non-steady mass accretion phenomena have also been suggested toward some of the protostellar sources through chemical diagnostics (e.g., Jørgensen et al. 2013; Sharma et al. 2020). The JCMT Transient Survey (Herzceg et al. 2017) has been monitoring ~ 295 submillimeter bright sources within the Gould Belt, finding 18 protostellar sources showing secular variabilities after four years of their survey (Lee et al. 2021). Furthermore, analysis of mid-infrared photometric monitoring observations by NEOWISE revealed that approximately 55% of protostars show variabilities in their flux with a timescale of within a day to years (Park et al. 2021). The fraction of variable sources is higher at the earlier evolutionary stages than at the later evolutionary stages, and the sources show either long-term secular variability (linear, curved, and periodic) or short-term stochastic variability (burst, drop, and irregular). Such variations are expected to be related to activities around the stellar surface and inner disk edge, which likely affect the mass accretion rate onto the star. Zakri et al. (2022) suggested that bursts from Class 0 protostars are as frequent, or even more frequent than those from the Class I protostars based on a long-term ($\gtrsim 15$ yr) systematic photometry study using Spitzer, WISE, and NEOWISE. Long term optical emission studies (~ 10 yr) toward T Tauri sources give us some hints of a possible link between the magnetospheric accretion and jet knots (e.g., time scale associated with 2-6 yr; Takami et al. 2020, 2023). All these studies demonstrate the importance of non-steady phenomena associated with the star-forming activities.

The millimeter source MMS1, driving the outflows and jets presented in this paper, is located in the Orion Molecular Cloud-3 region (OMC-3 region; $d=393$ pc by

Tobin et al. 2020¹). The region is known as one of the most active and young nearby intermediate-mass star-forming regions. There are 10 bright millimeter sources in the OMC-3 region (Chini et al. 1997; Lis et al. 1998) where several Class 0 and Class I sources were identified from the previous multi-wavelength and multi-line observations (e.g., Chini et al. 1997; Yu et al. 1997; Lis et al. 1998; Johnstone & Bally 1999; Aso et al. 2000; Stanke et al. 2002; Williams et al. 2003; Takahashi et al. 2006, 2008, 2009, 2012, 2013a; Takahashi & Ho 2012; Megeath et al. 2012; Stutz et al. 2013; Furlan et al. 2016; Tobin et al. 2020 and references therein).

MMS1 was first identified by the IRAM 30m telescope ($\theta \sim 11''$) in the 1.3 mm continuum band (Chini et al. 1997). MMS1 was also identified as CSO5 based on observations of SHARC/CSO in the 350 μm continuum band (Lis et al. 1998). Later the source was observed in the 850 μm continuum emission using the Submillimeter array ($\theta \sim 4''.5$) and named as SMM2 (Takahashi et al. 2013a). MMS1 is similarly bright as other (sub)millimeter sources in the OMC-3 region, which already host known protostars (Chini et al. 1997; Lis et al. 1998; Takahashi et al. 2013a). The flux concentration ratio of ~ 0.3 measured by Takahashi et al. (2013a), which compares fluxes measured from the JCMT $14''$ and SMA $4''.5$ beams, is comparable with these other protostellar sources, indicating that a similar amount of material has already condensed at the center of the core. Nevertheless, the source was not identified in the Herschel Orion Protostar Survey (HOPS survey) since no bright near- and mid-infrared compact and isolated emission was detected toward MMS1 at wavelengths $\lesssim 70 \mu\text{m}$ (Megeath et al. 2012; Furlan et al. 2016). No centimeter jet nor outflow has been reported toward MMS1 as yet (Reipurth et al. 1999; Takahashi et al. 2008). Based on these facts, MMS1 has been considered to be either at the end of the prestellar phase, the first core phase, or the earliest protostellar phase.

¹ The distance to the Orion A molecular cloud region is measured in several independent experiments: $414 \pm 7 \text{ pc}$ (Menten et al. 2007) and $389^{+24}_{-21} \text{ pc}$ (Sandstrom et al. 2007) using non-thermal radio emission in the Orion Nebula, $437 \pm 19 \text{ pc}$ (Hirota et al. 2007) and $416 \pm 6 \text{ pc}$ (Kim et al. 2008) using masers toward Orion KL; $398 \pm 7 \text{ pc}$ using centimeter radio source toward Orion A molecular complex (Kounkel et al. 2017), and $389 \pm 3 \text{ pc}$ using APOGEE-2 and *Gaia* DR2 (Kounkel et al. 2018) and 393 pc (Tobin et al. 2020) using *Gaia* DR2 toward Orion A complex. There are no direct distance measurements toward MMS1/OMC-3, we therefore rely on the nearby sources that have reliable parallax measurements. In this paper, Tobin et al. (2020) was adopted. All the measurements are consistent within $\sim 10\%$ of the adopted value.

With the improved angular resolution and sensitivity achieved with ALMA, for the first time, we have detected a very compact outflow and jet associated with MMS1 in both SiO (5–4) and CO (2–1) emission, respectively. We conclude that MMS1 is in the extremely early evolutionary Class 0 stage even without association of a bright mid-infrared source. Studying the velocity structure of the jet, we find evidence of intermittent mass ejection within the MMS1 jet. We present these results in this paper.

This paper is organized as follows. The observations are described in Section 2. The results including the 1.3 mm continuum, CO (2–1), and SiO (5–4) data sets are described in Section 3. The velocity structure of the outflow and jet, and comparison with magnetohydrodynamic (MHD) simulations are described in Section 4. Finally, concluding remarks and future prospects are given in Section 5.

2. OBSERVATIONS AND DATA REDUCTION

The ALMA observations were made in Cycle 3, 2016 January 29 (low angular resolution) and 2016 September 18 and 19 (high angular resolution) using the 1.3 mm band (Band 6). The phase center was set toward the location of the millimeter source, MMS1: R.A. (J2000) = $5^{\text{h}}35^{\text{m}}18^{\text{s}}.03$, decl. (J2000) = $-05^{\circ}00'17''.770$. The observing parameters are listed in Table 1. Total on-source time is about 16 minutes with ~ 40 antennas (high-angular resolution) and 4 minutes with 48 antennas (low-angular resolution). The low- and high-angular resolution data sets cover projected baselines between 8.5 k λ and 239 k λ and between 8.9 k λ and 2416 k λ , respectively. According to the ALMA proposer’s guide, the maximum recoverable scale (MRS) of the low- and high-angular resolution data is approximately $\sim 9''.8$ and $\sim 2''.0$, respectively. We observed CO ($J=2-1$) and SiO ($J=5-4$) at the velocity resolutions of 0.37 km s^{-1} and 0.39 km s^{-1} per channel, respectively. Line free channels corresponding to the effective band width of 454 MHz are allocated for imaging the continuum data. The Common Astronomy Software Application (CASA; CASA team et al. 2022) version 4.6.0 and version 4.7.0 were used as the standard ALMA data reduction for the low- and high-angular resolution data sets, respectively.

After calibration, the CLEANed images were made using the CASA task “`tclean`”. The Briggs weighting with robust parameter of 0.5 were used for the final images. The velocity width of 5.0 km s^{-1} was used in order to produce the CO and SiO image cubes both for high- and low-angular resolution data sets. The resulting synthesized beam sizes and 1σ rms noise levels for the CO,

SiO, and the 1.3 mm continuum emission are listed in Table 1.

3. RESULTS

We present the 1.3 mm continuum, CO(2–1), and SiO(5–4) emission maps obtained with the ALMA observations in this section. In this paper, the terminologies of “outflow” and “jet” use the following definitions. The outflow shows as relatively low velocity gas ($|v_{\text{LSR}} - v_{\text{sys}}| \lesssim 50 \text{ km s}^{-1}$), and wide opening angles. The jet shows as high velocity outflow gas ($|v_{\text{LSR}} - v_{\text{sys}}| \gtrsim 50 \text{ km s}^{-1}$), and a collimated structure. The jets are located within the outflow lobes. The systemic velocity of 11 km s^{-1} is adopted for the system, which is determined from the optically thin molecular lines in the OMC-3 region (e.g., Takahashi et al. 2009; Matsushita et al. 2019; Morii et al. 2021a).

3.1. The 1.3 mm Continuum Emission

Figure 1 shows the 1.3 mm continuum emission toward MMS1 obtained with ALMA. We have detected centrally concentrated continuum emission both in the low- and high-angular resolution images. Note that the origin of the 1.3 mm continuum emission observed toward the protostellar sources in OMC-3 is considered to be significantly dominated by the thermal dust emission. The emission attributed to the free-free emission, tracing ionized jets, is likely negligible as estimated by Takahashi et al. (2006, 2009, 2013a, 2019).

In order to characterize the source structure, particularly the centrally concentrated emission, presumably tracing the dust disk, we performed two-component two dimensional (2D) Gaussian fitting on the high-angular resolution image. The residual level of the fitting result is less than 5.6% with respect to the observed peak flux (i.e., the residual level is less than $S/N = 2.5$). The source structure was fitted by an extended ($\sim 750 \pm 47 \text{ au} \times 510 \pm 33 \text{ au}$) and a compact ($\sim 43 \pm 5.1 \text{ au} \times 26 \pm 4.7 \text{ au}$) Gaussian component, both of which are listed in Table 2. The position angle² (p.a.) of the major axis of both extended and compact components ($150^\circ \pm 7.5^\circ$ and $156^\circ \pm 12^\circ$, respectively) are roughly aligned to the direction of the large-scale filament in this region (i.e., Chini et al. 1997; Johnstone & Bally 1999; p.a. $\sim 135^\circ$). The orientation of the compact component is almost perpendicular to the molecular jet detected with ALMA in the SiO emission (Section 3.3). Assuming that the detected compact 1.3 mm continuum emission traces the dust disk, an inclination angle of the

disk (i) is estimated to be $\sim 53^\circ$ using the axis ratio of the 1.3 mm continuum compact component. Note that the millimeter continuum fitting was also performed by Liu et al. (2023) as a part of the full polarization data analysis. The data were obtained in the 1.1 mm band. A slightly higher angular resolution than that presented here of $0''.14$ was achieved with a factor of 6.8 better sensitivity for the full polarization data presented. Despite the significant sensitivity differences, the total flux measured within the compact component is consistent within the factor of ~ 1.2 . The measured size of the disk-like structure in this paper is factor of ~ 4.5 larger (in terms of the surface area) than those estimated in Liu et al. (2023). This is likely due to the factor of ~ 1.7 larger beam size (in terms of the beam surface area) in the data set presented here compared with that presented in Liu et al. (2023) to ApJ.

The mass of the circumstellar material can be estimated from the 1.3 mm continuum emission using the following equation,

$$M_{\text{H}_2} = \frac{F_\lambda d^2}{\kappa_\lambda B_\lambda(T_d)}, \quad (1)$$

where F_λ is the total 1.3 mm flux, d is the distance to the source, κ_λ is the dust opacity (absorption coefficient per unit gas mass). Here, a gas-to-dust mass ratio of 100 is assumed. T_d is the dust temperature, and $B_\lambda(T_d)$ is the Planck function at a temperature of T_d . Assuming, $d = 393 \text{ pc}$ (distance to the OMC-3 region measured from the *Gaia* DR2 data; Tobin et al. 2020; McBride & Kounkel 2019; *Gaia* Collaboration et al. 2018), $\kappa_{1.3\text{mm}} = 0.011 \text{ cm}^2 \text{ g}^{-1}$ from the dust coagulation model of the MRN (Mathis et al. 1977) with thin ice mantles at a number density of 10^8 cm^{-3} (Ossenkopf & Henning 1994), $T_{\text{dust}} = 30 \text{ K} - 100 \text{ K}$ (e.g., Nomura & Millar 2005; Tomida et al. 2017), and given the measured total fluxes listed in Table 2, the masses of the compact and extended components are estimated to be $M_{\text{H}_2(\text{comp.})} \sim 0.0051 - 0.020 M_\odot$ and $M_{\text{H}_2(\text{ext.})} \sim 0.041 - 0.16 M_\odot$, respectively. Note that the dust temperature assumption was discussed by Liu et al. (2023) in detail based on recent studies toward Orion protostars by Tobin et al. (2020) and Xu & Kunz (2021) considering the stellar radiation and disk accretion heating, respectively. The minimum and maximum temperatures adopted here are comparable to the temperature assuming the stellar radiation expected from the given radius corresponding to the extended and compact structures.

3.2. CO and SiO Line Profiles

Figure 2 presents comparisons of the missing flux measured in the CO and SiO images obtained from the low

² The position angle is measured from the north to the east with respect to the blue-shifted lobe.

Table 1. Observing Parameters

Parameter	High-resolution Data	Low-resolution Data
Observing date (YYYY-MM-DD)	2016-09-18 and -19	2016-01-29
Number of antennas	38, 40	48
Primary beam size (arcsec)	27	27
PWV (mm)	1.1 – 2.2	~2.6
Phase stability rms (degree) ^a	21 – 52	~13
Bandpass calibrators	J0510+1800	J0522-3627
Flux calibrators	J0510+1800, J0522-3627	J0522-3627
Phase calibrators ^b	J0607-0834	J0541-0541
Spectral line setups USB/LSB (GHz)	230.535; 231.319 / 217.102; 219.557	
Total continuum bandwidth; USB+LSB (MHz)	454	454
Projected baseline ranges (kλ)	8.9 – 2416	8.5 – 239
Maximum recoverable size (arcsec)	~2.0	~9.8
Total on-source time (minutes)	16	4
Synthesized beam size of the CO (2–1) images (arcsec)	0.18×0.15 (p.a.=−18deg.)	1.5×0.9 (p.a.=−78deg.)
Synthesized beam size of the SiO (5–4) images (arcsec)	0.21×0.17 (p.a.=−27deg.)	1.6×0.9 (p.a.=−78deg.)
Synthesized beam size of the continuum images (arcsec)	0.19×0.16 (p.a.=−25deg.)	1.6×0.9 (p.a.=−77deg.)
RMS noise level of the CO (2–1) images (mJy beam ^{−1} km s ^{−1}) ^c	2.7	3.8
RMS noise level of the SiO (5–4) images (mJy beam ^{−1} km s ^{−1}) ^c	1.8	3.4
RMS noise level of the continuum images (mJy beam ^{−1})	0.24	0.55

^a Antenna-based phase differences on phase calibrators.

^b The phase calibrator was observed every 8 minutes.

^c RMS noise levels measured with the velocity width of 5 km s^{−1}.

Table 2. Two Dimensional Gaussian Fitting Results obtained from the 1.3 mm Continuum Emission

	R.A. (J2000)	Decl. (J2000)	Deconvolved Size, p.a. (arcsec, degree)	Peak Intensity (mJy beam ^{−1})	Flux Density (mJy)
Compact component	05 ^h 35 ^m 18 ^s .0525±0.0019''	−05° 00′ 17''.980±0.0027''	0''11±0''.013×0''.065±0''.012, 156±12	9.4±0.25	12 ± 0.51
Extended component	05 ^h 35 ^m 18 ^s .0537±0.0400''	−05° 00′ 18''.167±0.048''	1''.9±0''.12×1''.3±0''.085, 150±7.5	1.1±0.073	96 ± 6.2

resolution ($\theta\sim 1''.5$) and high resolution ($\theta\sim 0''.2$) images. The comparisons show that the fluxes obtained from the two data sets are almost the same. Thus, there is no significant missing flux in the high angular resolution data set. The missing flux comparisons imply that a majority of the flux originating from the outflow and the jet, traced by CO (2–1) and SiO (5–4), came from compact structures that are packed within the MRS of the high-angular resolution data ($\sim 2''.0$). Since no significant missing flux was reported particularly, in the mid- and high-velocity ranges for both CO and SiO emissions, we only use the high angular resolution images in this paper.

We note discrete flux enhancements both in CO (2–1) and SiO (5–4) at the high velocity range of $|v_{\text{LSR}} - v_{\text{sys}}| \approx 50 \text{ km s}^{-1}$. These line profiles show clear evidence of the extremely high velocity (EHV) flow which was first discovered by [Bachiller & Cernicharo \(1990\)](#) toward NGC 1333 (HH 7-11), and then was reported for several low- and intermediate-mass Class 0 sources ([Bachiller et al. 1991a,b, 2000](#); [Zapata et al. 2005](#); [Hirano et al.](#)

[2010](#); [Gómez-Ruiz et al. 2013, 2019](#); [Tafalla et al. 2017](#); [Lee et al. 2017](#); [Matsushita et al. 2019](#); [Lee 2020](#)). Together with recent studies of the compact EHV flow toward MMS 5 by [Matsushita et al. \(2019\)](#), and MMS 6 [Takahashi et al. \(2012\)](#), [Takahashi et al. \(2019\)](#), and [Takahashi et al. \(2024 in prep.\)](#), the EHV flow associated with MMS 1 is one of the most compact EHV flows ever reported (see Section 3.3). Note that, hereafter, the terminology of “jet (or SiO jet)” will be used to refer to the EHV flow.

3.3. Outflow and Jet

We present the ALMA CO (2–1) and SiO (5–4) emission arising from the outflow and jet located in MMS 1 in Figure 3. A compact molecular outflow is traced by the CO emission, and a collimated high-velocity jet within the outflow is traced by the SiO emission. Both outflow and jet associated with MMS 1 were, for the first time, detected thanks to the ALMA’s sensitivity and high-angular resolution capabilities. This clearly indicates that MMS 1 contains a protostar. The blue- and

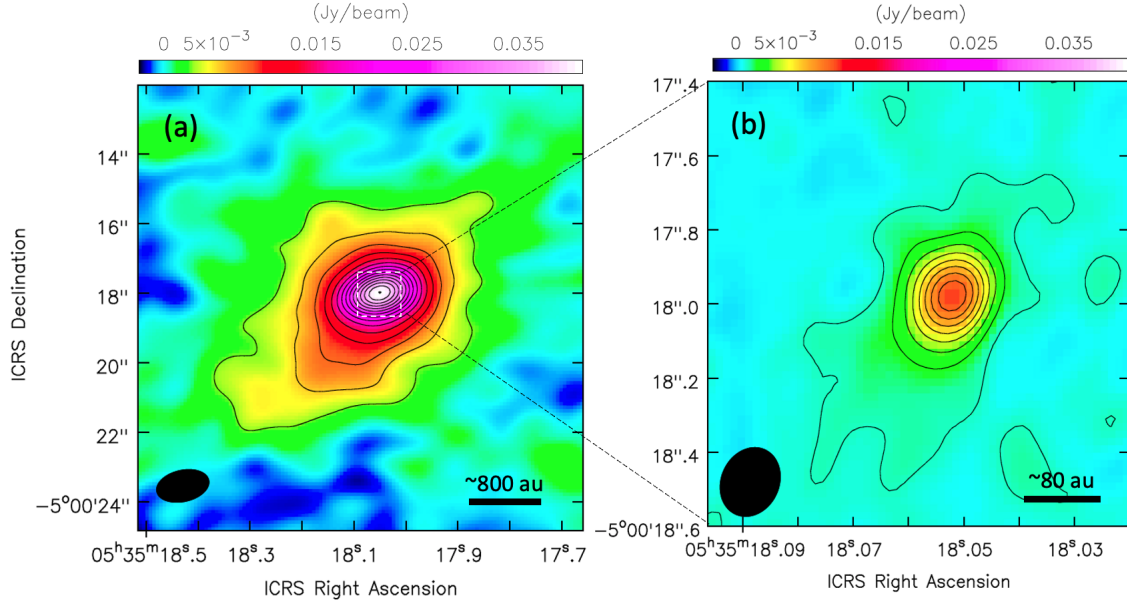


Figure 1. The 1.3 mm continuum emission toward MMS 1 obtained from ALMA observations with low angular resolution (a) and high angular resolution (b). Contour level starts from 5σ with an interval of 5σ up to 70σ for panel (a) and up to 40σ for panel (b).

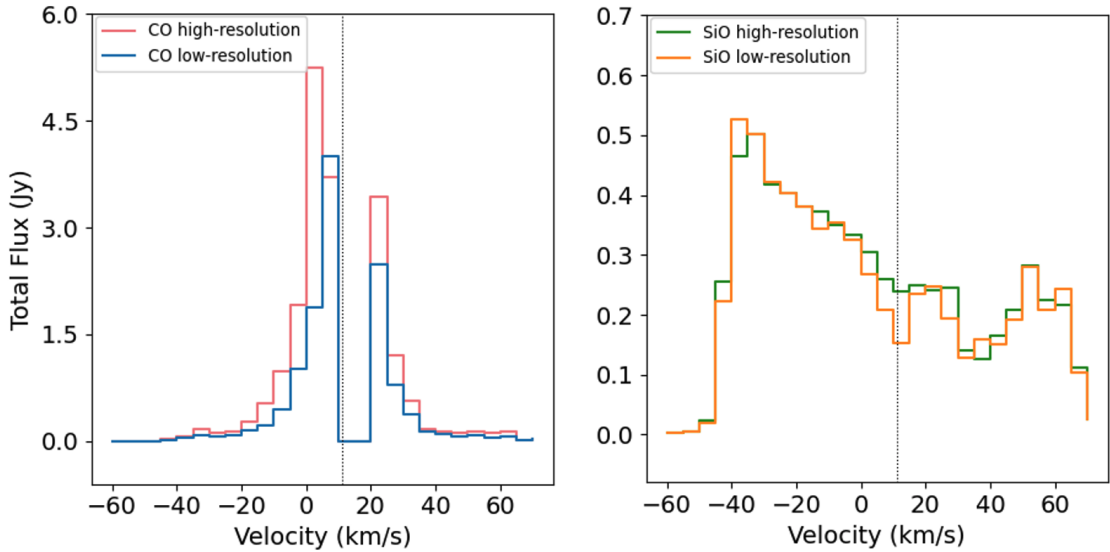


Figure 2. Line profiles of MMS 1 obtained from the CO (2–1) and SiO (5–4) emission, respectively. Comparisons of the fluxes measured from the low- and high-angular resolution images are presented. The high resolution images are convolved with the low resolution beam size using the CASA task “*imsmooth*”. Then, the images are re-gridded with “*imregrid*”. Finally, flux measurements are performed for each channel using the area having greater than 5σ detection in the high angular resolution images. The systemic velocity of 11 km s^{-1} is noted in the vertical dotted line in each panel.

red-shifted gas are located in the southwest (SW) and northeast (NE) directions with respect to the millimeter source peak, respectively, with the position angle of -137° . As seen in Figure 3b, the axis of the CO outflow and SiO jet is aligned more or less perpendicular to

the disk-like structure traced in the 1.3 mm continuum emission. As clearly seen in Figure 3a, the jet traced in the SiO emission shows a wiggled structure.

Figures 4a, b, and c present moment maps obtained from the CO (2–1) emission. The CO blue- and red-

shifted lobes are extended up to $\sim 3''.2$ (~ 1260 au) and $\sim 5''.1$ (~ 2000 au), respectively. The CO emission is detected with the LSR velocity range between -35 and 60 km s^{-1} . Figure 4c shows that the majority of the gas detected in CO (2–1) emission has a velocity dispersion of $|v_{\text{LSR}} - v_{\text{sys}}| \lesssim 7 \text{ km s}^{-1}$. An X-shaped structure associated with central protostar, tracing the outflow cavity is clearly seen. The width of the outflow, where the outflow has the widest width in both lobes, is measured to be $\sim 1''.3$ (~ 510 au).

As presented in Figures 4d, e, and f, the collimated jet is detected in SiO (5–4) emission with the projected length of $\sim 2''.3$ (~ 900 au; blue-shifted emission) and $\sim 1''.3$ (~ 510 au; red-shifted emission), respectively. The SiO emission was detected with the LSR velocity between -60 and 70 km s^{-1} . Velocity tendency is consistent with that observed in CO, while the SiO emission mainly tracing the high-velocity collimated jet rather than the wide-opening angle outflow seen in CO. Note that the SiO emission is located close to the central star, in particular the blue-shifted component shows a width comparable to the CO outflow (Figure 3b and 4e). This wide width SiO emission distribution is only seen in the relatively low-velocity (the LSR velocity between -15 km s^{-1} and 5 km s^{-1}), tracing the outflow cavity. Within the outflow cavity, we see a high-velocity collimated jet.

The detected high-velocity SiO emission traces two components: (i) emission associated with the central region, showing a collimated structure and (ii) bullet-shaped emission (i.e., bow-shocks as explained using Figure 5 in the following paragraph) located at the tips of the CO outflow. The first component traces a collimated jet and is slightly brighter on the SW side (blue-shifted emission) than on the NE side (red-shifted emission). The spatially resolved image (Figure 4d) reveals that the jet appears to wiggle, and that the SW side of the jet contains at least three bright knots (and an additional faint knot as presented in Figure 6). The second component, showing the bullet-shaped structure, is located at $\sim 6''.2$ (~ 580 au; blue-shifted emission) and $\sim 2''.0$ (~ 790 au; red-shifted emission) away from the 1.3 mm continuum peak position and brighter in the NE side (red-shifted emission) than in the SW side (blue-shifted emission). The location of the SiO bullet-shaped structure roughly coincides with the tips of the outflow lobes observed in the CO emission. The associated gas velocity is lower than that observed in the jet. The blue-shifted emission is detected in the LSR velocity range between -10 and -40 km s^{-1} , and the red-shifted emission is detected in the LSR velocity range between 10 and 30 km s^{-1} (Figure 4 and 5). Velocity dispersions of $\Delta v \sim 10 \text{ km s}^{-1}$ and $\Delta v \sim 4 \text{ km s}^{-1}$ are observed toward

the blue-shifted and the red-shifted bullet-shaped emission, respectively (Figure 4f).

Figure 5 presents the position-velocity diagram (PV-diagram) obtained from the CO (2–1) and SiO (5–4) data cubes cut along the outflow axis (p.a. = -137°). Clearly seen in the PV-diagram, there are two distinct components: (i) a collimated jet and (ii) the bullets located at the tips of the CO outflow. Regarding the first component (i), SiO emission is concentrated in the central $2''$ region, showing a linear velocity increase with respect to distance from the center. The right panel of Figure 5 presents the zoomed image of the jet, which clearly shows that there are at least three components (as denoted by colored lines) showing similar respective velocity increases. This is particularly clear in the blue-shifted jet (i.e., SW side). The terminal point of each component coincides with an emission peak, which also corresponds to individual knots indicated in Figure 4d. Regarding the second component (ii), the SiO emission is located at the tips of the CO blue- and red-shifted outflows. The spatial and velocity patterns in the PV-diagram are consistent with those explained with the jet bow-shock model presented in Figure 2 of Arce et al. (2007). Consistent with what we see in Figure 4b and c, the CO emission in Figure 5 mainly traces the low- to intermediate-velocity gas components ($|v_{\text{LSR}} - v_{\text{sys}}| \lesssim 20 \text{ km s}^{-1}$). These components are spatially extended and mostly associated with the outflow cavity and lobes. The CO emission is also detected toward the bow-shocks, and is particularly bright in the red-shifted emission component (i.e., NE side).

3.4. Timescales

In this subsection, we estimate two types of timescales: (i) outflow and jet dynamical timescales, which represent how young the protostar is, and (ii) dynamical timescales to each knot, which is possibly related to the time interval of the episodic mass ejection within the jet.

3.4.1. Outflow and Jet Dynamical Timescales

Two velocity components are seen in the PV-diagram mainly obtained from the SiO (5–4) emission presented in Figure 5. The first one is the SiO emission associated with a collimated jet, and the second one is the emission located at the tips of the outflow lobes, tracing bow-shocks. The dynamical timescale of the outflow and jet, t_{dyn} , are estimated using the distance to the bow-shocks and length of the SiO jet, respectively. Gas velocities measured in each location were used for the calculations as following,

$$t_{\text{dyn}} = \left(\frac{l_{\text{obs}}}{v_{\text{obs}}} \right) \left(\frac{\cos i}{\sin i} \right), \quad (2)$$

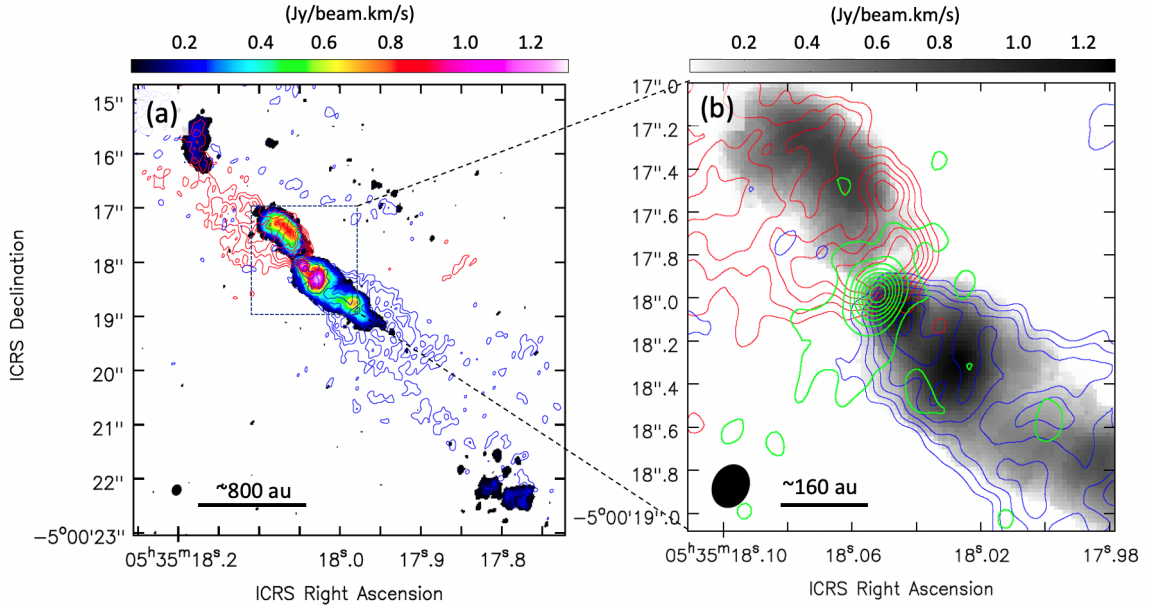


Figure 3. (a) Integrated intensity image obtained from the CO (2–1) red- and blue-shifted components (red- and blue-contours) with the v_{LSR} velocity integrated over -45 to 10 km s^{-1} and 15 to 60 km s^{-1} , respectively. Contour levels are 20%, 30%, 40%, 50%, 60%, and 70% with respect to the peak intensity of the blue- and red-shifted CO integrated images. An integrated intensity image obtained from the SiO (5–4) is shown in color with the v_{LSR} velocity integrated over -60 to 70 km s^{-1} . (b) Zoomed in image of panel (a). The 1.3 mm continuum emission is presented in green contours. Contour level starts from 5σ with an interval of 5σ up to 40σ ($1\sigma=240 \text{ mJy beam}^{-1}$). SiO integrated image is presented in the grey scale instead of the color used in panel (a). The synthesized beam size is denoted in the bottom left corner of each panel.

where l_{obs} and v_{obs} are the projected jet and outflow lengths and the line of sight gas velocities, and i is the inclination angle of the jet and outflow with respect to the line of sight. Here, we adopt $i = 45^\circ$, estimated from the axis ratio of the dust disk by Liu et al. (2023). Given the SiO jet lengths (l_{obs}) of 900 au (blue-shifted) and 510 au (red-shifted side) measured from the first-moment map presented in Figure 4d, and the maximum gas velocities (v_{obs}) at the tip of the jet of 65 km s^{-1} (blue-shifted emission) and 44 km s^{-1} (red-shifted emission) measured from the first-moment map presented in Figure 4e, the jet dynamical timescale is estimated to be 66 yr (blue-shifted jet) and 55 yr (red-shifted jet), respectively. For the molecular outflow, we assume that the outflow emission is extended up to the locations of the bow-shocks, which correspond to the extension of the CO outflow. Given the outflow lengths (l_{obs}) of 2460 au (blue-shifted side) and 1260 au (red-shifted side), and the maximum gas velocities (v_{obs}) measured from the SiO bow-shocks, presented in Figure 4e, of 33 km s^{-1} (blue-shifted emission) and 9 km s^{-1} (red-shifted emission), the outflow dynamical timescales are estimated to be 350 yr (blue-shifted side) and 660 yr (red-shifted side), respectively. Note that the inclination angle, i , of the disk-like structure derived from the 1.3 mm continuum emission is $\sim 53^\circ$. Adopting $i = 53^\circ$ makes the change in jet/outflow

lengths and velocities of a factor of ~ 1.1 smaller and ~ 1.2 larger with respect to the current assumptions, respectively. This introduces the timescale estimations of a factor of ~ 1.4 longer than the current estimations.

The short dynamical timescales of the outflow and jet are reported by Matsushita et al. (2019) toward MMS 5/ OMC-3, which are 1300 yr and 110 yr, respectively. The dynamical timescales estimated for MMS 1 are even shorter than those values. In addition, a similar compact outflow has been reported toward MMS 6/OMC-3, which has the dynamical timescale of ~ 50 yr (Takahashi & Ho 2012). The dynamical timescale of the SiO jet detected in MMS 1 is as short as that of the outflow detected toward MMS 6.

3.4.2. Dynamical Timescale to Each SiO Knot

As presented in Figure 4d and discussed further below in Section 4.1, we have detected periodic flux enhancements within the SiO jet, which are considered to be associated with knots and possibly related to episodic mass ejection events. Figure 6 presents the map of a representative velocity channel ($v_{\text{LSR}} \sim 40 \text{ km s}^{-1}$), showing four bright knots detected within the blue-shifted SiO jet. Dynamical timescales toward each knot are calculated using the distance between the central source (i.e., millimeter peak position) and the flux peak of each knot, and the maximum gas velocity associated with

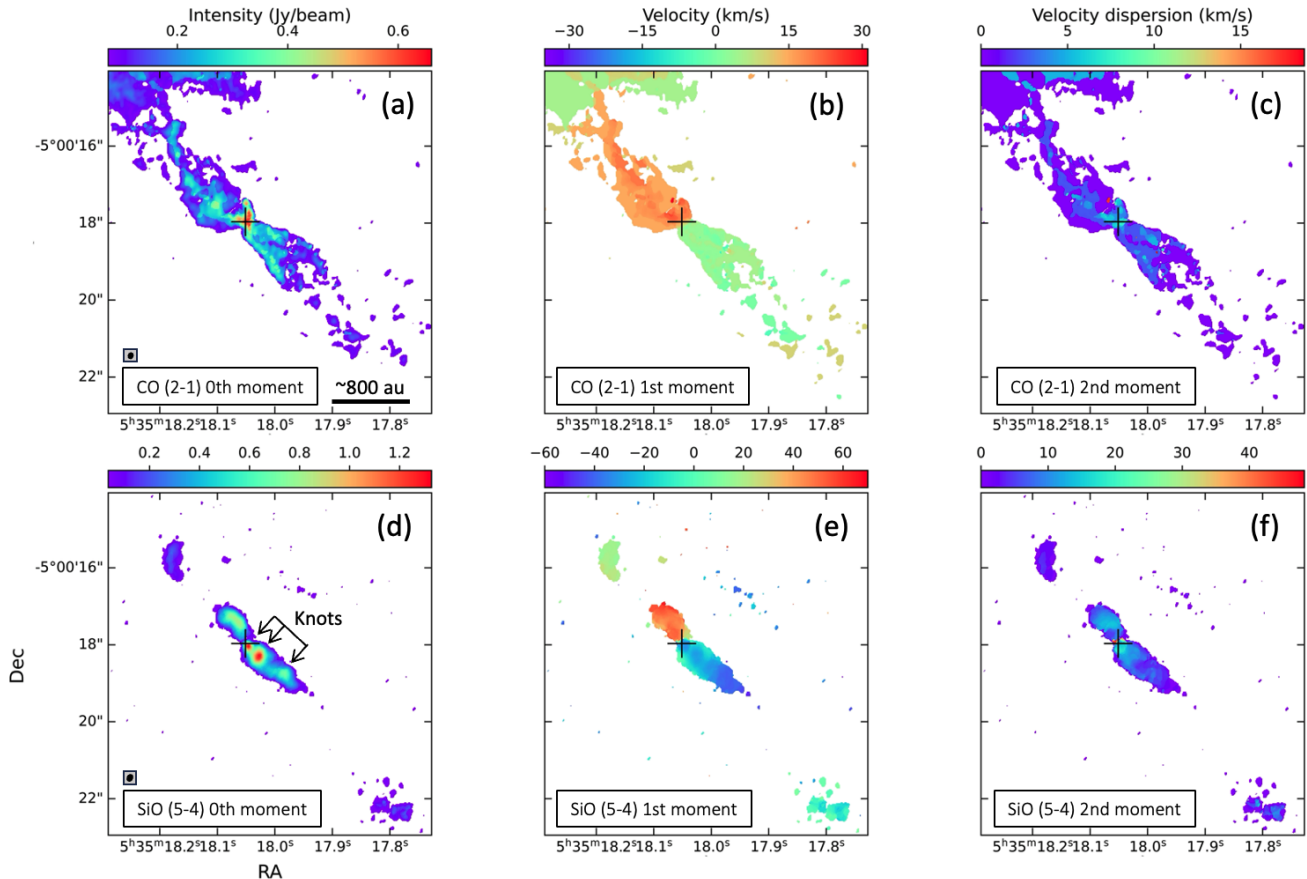


Figure 4. The zeroth-, first-, and second-moment maps of MMS 1 obtained from the CO (2–1) and SiO (5–4) emission. The moment maps were made using the CASA task ‘‘immoments’’. No clip and a clip level of $0.007 \text{ Jy beam}^{-1}$ was applied for CO (2–1) and SiO (5–4), respectively. Location of the 1.3 mm continuum peak position is denoted by the cross mark in each panel. A linear size scale is denoted in the right bottom corner of panel (a), and the synthesized beam size of the CO and SiO observations are denoted in the bottom left corner of panels (a) and (d), respectively.

each component measured from the PV-diagram (Figure 5), which are 5 yr (K1), 18 yr (K2), 45 yr (K3), and 53 yr (K4) after applying the inclination correction (i.e., $i=45^\circ$ estimated by Liu et al. 2023).

3.5. Jet Precession

We showed evidence for jet wiggling in Section 3.3 (Figure 3a). In general, jet wiggling can be explained either by orbital motion of a binary system (Masciadri & Raga 2002) or by jet precession (or precession of the jet-driving object; Frank et al. 2014). Both models produce a ‘‘garden-hose’’ effect, resulting in jet wiggling (Raga et al. 1993). The observed MMS 1 jet morphology allows us to distinguish the origin of the jet wiggling (Frank et al. 2014; de A. Schutzer et al. 2022, and references therein). In the case of jet wiggling due to binary orbital motion, the jet is expected to bend in the direction opposite to the location of the secondary (binary) component. This produces a V-shaped jet in the vicinity of the protostar. The previously ejected gas propagates

within the cone-shaped structure, and the side-to-side wiggling over time produces a W-shaped structure in the projected jet locus. Alternatively, in the case of jet precession, the jet is expected to be ejected symmetrically. Side-to-side moving gas within the cone therefore produces an S-shaped locus over time.

The SiO jet ejected from MMS 1 shows an S-shaped wiggle. Furthermore, at the current angular resolution of $\sim 0''.15$ ($\sim 60 \text{ au}$ in the linear size scale), we did not find any evidence that MMS 1 is a binary system. These facts support that the jet wiggling associated with MMS 1 can be caused by the jet precession rather than the orbital motion of a binary system.

We fitted the wiggling jet observed in MMS 1 with a three dimensional spiral morphology using the following parametric equations (3), (4), and (5), as described by de A. Schutzer et al. (2022) and originally based on Raga et al. (1993) and Masciadri & Raga (2002);

$$x = z \tan \beta \sin \left(\frac{2\pi}{\lambda} |z| + \phi \right), \quad (3)$$

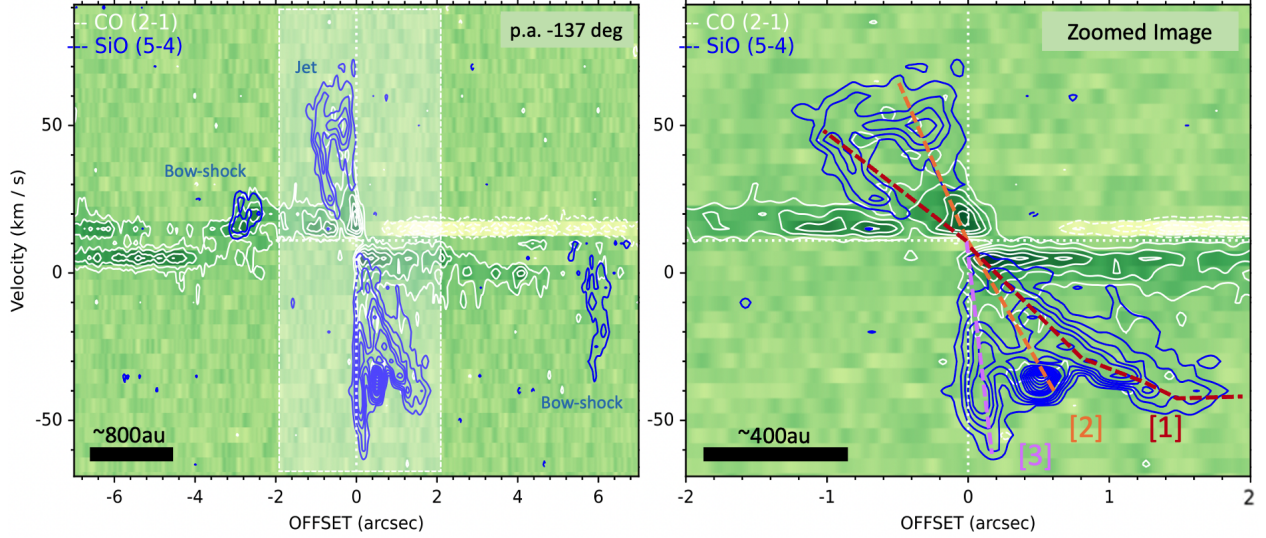


Figure 5. Position-Velocity (PV) diagram cutting along the axis of the outflow (p.a. = -137°). The background color and white contours correspond to CO (2–1) emission. Contour levels starts from -9σ with an interval of 3σ up to 15σ . The SiO (5–4) emission is denoted in blue contours. Contour levels starts from -3σ with an interval of 3σ up to 33σ . Negative contours are denoted by the dashed lines. The left panel presents the entire PV diagram, while the zoomed in image within the white hatched area is presented in the right panel, which reveals the emission mainly from the protostellar jet. The vertical and horizontal dotted lines correspond to the location of the 1.3mm continuum emission peak and the system velocity of MMS 1 ($v_{\text{sys}}=11 \text{ km s}^{-1}$), respectively. Colored dashed lines denoted in the right panel are guide lines used for explaining the possible episodic mass ejection scenario discussed in Section 4.1. The length of the black solid line in the bottom left corner in each panel shows a linear scale, and the width of the line shows the velocity resolution of the presented SiO and CO data.

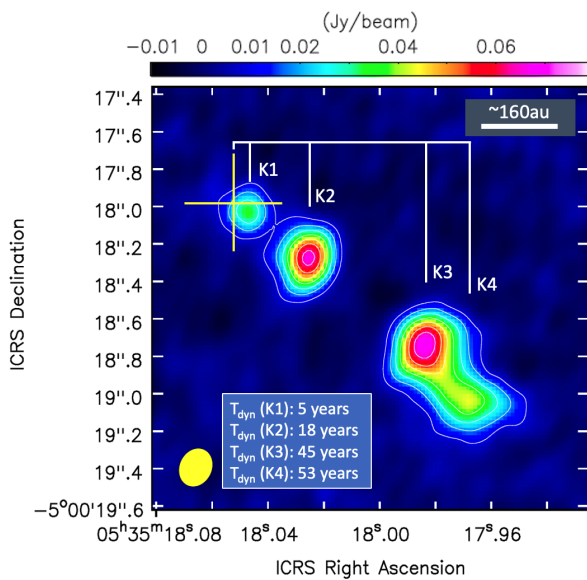


Figure 6. Four bright knots, K1, K2, K3, and K4, detected in SiO (5–4) emission within the jet. A representative velocity channel map of $v_{\text{LSR}}=-40 \text{ km s}^{-1}$ is presented here. Peak position of the millimeter emission is denoted by a yellow cross and dynamical timescales for each knot calculated in Subsection 3.4.2 are listed at the bottom left corner together with the synthesized beam size. Contour levels start from 5σ with an interval of 5σ up to 35σ ($1\sigma=1.8 \text{ mJy beam}^{-1}$).

$$y = z \tan \beta \cos \left(\frac{2\pi}{\lambda} |z| + \phi \right), \quad (4)$$

where we consider the situation that the jet precesses inside a cone of main axis z . Here, β is the jet half-opening angle, λ is the spatial period, and ϕ is the phase angle. The precession axis tilts at an inclination angle of i with respect to the plane of the sky. The projected coordinates (α', δ') in this plane are given by

$$(\alpha', \delta') = (y, z \cos i - x \sin i). \quad (5)$$

We adopted the inclination angle of the jet as 45° which is estimated from the disk axis ratio, as discussed in Section 3.4.1. Then, the other parameters of the jet position angle λ , β , and the phase angle ϕ were fitted simultaneously by eye. During the fitting process, we found that the northern and southern jets have different position angles of 35° and 51° , respectively, requiring an axis misalignment of 16° . Hence, the fitting was done independently for the northern and southern jets. The fitting results and parameters are presented in Figure 7 and Table 3, respectively. Although the axis is misaligned between the northern and southern jets, the fitted parameters are similar, indicating that the jet shows a more or less symmetric ejection.

Although the cause of the jet precession is not fully understood, a few possible scenarios have been proposed.

The first one is the tidal interaction between the associated protostellar disk and the noncoplanar binary companion, creating an S-shaped wiggle jet in the vicinity of protostars (Terquem et al. 1999). However, we did not find any apparent substructures within the central 100 au scale with the current angular resolution, as shown in Figure 1b. Thus, we can exclude the tidal interaction scenario.

Alternatively, recent simulation studies have demonstrated that the misalignment of the core rotation axis with respect to the global magnetic field can produce an S-shaped wiggling jet (Hirano & Machida 2019; Hirano et al. 2020; Machida et al. 2020). In their core-collapse simulations, the precession of the protostar and disk occurs when the prestellar core has a rotation axis that is not parallel with the global magnetic field. In our observations, a slight misalignment between the large-scale magnetic field (p.a. $\sim 45^\circ$) and both the disk rotation axis (i.e., perpendicular to the disk major axis, p.a. $\sim 65^\circ$) and the observed SiO jet axis (p.a. 35° for the northern jet and p.a. 51° for the southern jet) has been observed toward MMS 1, which could explain the jet precession observed in MMS 1.

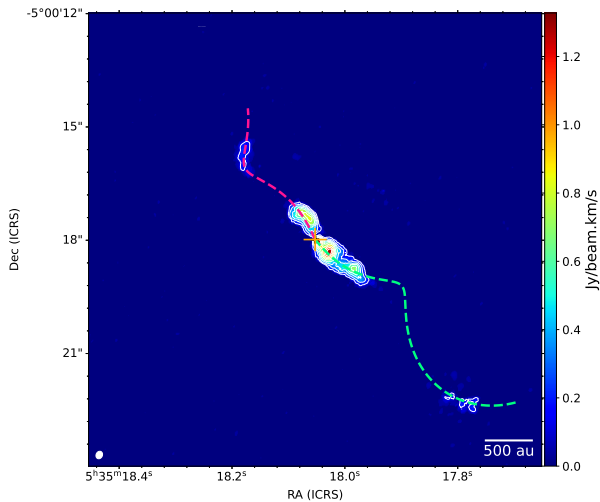


Figure 7. Integrated intensity image obtained from the SiO (5–4) emission overlaid with the jet precession model discussion in Section 3.5. Adopted models for the northern and southern jets are denoted in magenta and light green color, respectively. Contour level starts with 10% with an interval of 10% up to 90% with respect to the SiO peak intensity. Location of the 1.3mm dust continuum peak is marked in the orange cross. Synthesized beam is denoted in the bottom left corner.

4. DISCUSSION

The molecular outflow and jet associated with MMS 1 are detected for the first time with the high-angular resolution and the high-sensitivity capabilities of ALMA. The detected jet is the smallest thus far reported, hence a good opportunity to look into the initial mass ejection phenomena from a protostar. As presented in Figure 5, the jet velocities linearly increase as the distance from the center increases. In addition, Figure 6 indicates the possibility of episodic mass ejection events. In this section, we discuss possible origins of the velocity structure by comparing the observational results with MHD simulations (Subsection 4.1). Then, we discuss how the presented dynamical model relates to those features traced by the SiO emission (Subsection 4.2). Finally, we discuss the intermittent mass ejection phenomena and how this may be related to episodic mass accretion, which has previously been reported for several protostars (Subsection 4.3).

4.1. Comparison between Observation and Simulation

To further validate the acceleration of the jet in MMS 1 seen in Figure 5, we compare a recent numerical simulation of protostar evolution with our results. The data in Figure 8 were taken from the core collapse simulation performed by Machida & Basu (2019).

We first explain the numerical settings and detailed simulation results by Machida & Basu (2019), for which a spherical core with a Bonnor-Ebert density profile was adopted as the initial state. The radius R_{cl} and mass M_{cl} of this initial cloud core are $R_{cl} = 1.2 \times 10^4$ au and $M_{cl} = 1.7 M_\odot$. A uniform magnetic field with $B_0 = 4.5 \times 10^{-5}$ G and a rigid rotation of $\Omega_0 = 1.1 \times 10^{-13}$ rad s $^{-1}$ were added to the initial state. The gravitational collapse of the core was calculated using a nested grid method (Machida et al. 2004; Machida & Hosokawa 2013), in which the resistive magnetohydrodynamics equations (see, eqs. [1]–[7] in Machida & Matsumoto 2012) were solved. The finest spatial resolution of the simulation is 5.6×10^{-3} au. As a result, both the star-forming core ($\sim 10^4$ au) and the protostar (~ 0.01 au) were spatially resolved in the simulation. Starting from the prestellar core, the evolution of the system is calculated for 2000 yr after protostar formation.

The simulation produces episodic jets driven from the inner disk region (see Fig. 2 of Machida 2014). These jets with speeds ~ 100 km s $^{-1}$ appear repeatedly every $\sim 1 - 10$ yr until the end of the simulation 2000 yr after protostar formation. In the following analysis, we consider the simulation result between 200.21–201.69 yr after protostar formation, during which the high-speed jet appears three times, as shown in Figure 8. Although

Table 3. Parameters of jet precession model

Parameter	λ ($''$)	v_{jet} (km s^{-1})	β ($^{\circ}$)	$t_{\text{prec.}}$ (yr)	ϕ ($^{\circ}$)
North	7.8	62	7.0	234	174
South	6.8	92	8.0	138	180

Notes. The jet velocity was measured from the SiO observations. The values measured from the first-moment map (see Section 3.4.1) were used to calculate the jet velocities with $v_{\text{jet}}=v_{\text{obs}}/\sin i$ (with $i=45^{\circ}$).

the full simulation reveals a wide range of mass ejection rates due to the jets ($\sim 10^{-6} - 10^{-9} M_{\odot} \text{ yr}^{-1}$, see Fig. 7 of Machida & Basu 2019), the mass ejection rate during the epoch shown in Figure 8 is about $3 \times 10^{-6} M_{\odot} \text{ yr}^{-1}$.

In Figure 8, the density and velocity distributions on the $y = 0$ plane (left) and the PV diagram along the jet or z -axis (right) at three different epochs, 200.21, 200.58, and 201.69 yr after protostar formation are plotted. As described above, the simulation spatially resolved the protostar and circumstellar disk and reproduced the outflow and jet. Thus, we can qualitatively compare the kinematics of the observed jet with the simulation. The left panels of Figure 8 show that the high-velocity flow, with several local density peaks, is surrounded by the low-velocity flow (for details, see Machida & Basu 2019). The right panel of Figure 8 plots the PV-diagram at each epoch, in which we only used the simulation data around the z -axis as $-5 \text{ au} \leq x \leq 5 \text{ au}$ and $-5 \text{ au} \leq y \leq 5 \text{ au}$ to create the PV-diagram (the white dashed line in panels (a), (c), and (e)) in order to focus on the high-velocity component (i.e., the jet).

In the second and fourth quadrants of the PV diagram in Figure 8b, we can confirm several spine-like components. Each spine corresponds to a clump ejected from the region near the protostar. We can see a weak density peak at $z \simeq \pm 20 \text{ au}$ within the white dashed line of Figure 8a which corresponds to the clump produced during a previous mass ejection event occurring 197.18 years after protostar formation. In the PV diagram (Figure 8b), we can also confirm the jet intermittent components at $z = \pm 20 \text{ au}$, corresponding to the clump made during the previous ejection event, which is labeled as [1]. In addition, a strong mass ejection is currently occurring at the root of the jet. A sharp spine around $z \simeq 0$ in the PV diagram (Figure 8a) labeled as [2] corresponds to the current mass ejection event close to the protostar. The color in the PV diagram representing the launching radius of each velocity component indicates that the jet launching radii are widely distributed across the range of 0.01-1 au. We confirmed that various velocity components in the range $< 150 \text{ km s}^{-1}$ appear at every mass ejection event. The mass ejection occurs at different disk

radii and the gas ejected at different radii has different velocities. Thus, a sharp spine appears around $z = 0$ in the PV diagram immediately after the mass ejection occurs. Note that mass ejection recurrently occurs in the main accretion phase (Machida & Basu 2019).

The spine labeled as [2] widens and is inclined from the vertical axis in Figure 8(d). In addition, we can confirm that the jet velocity labeled as [2] linearly increases as the distance from the protostar increases in Figure 8(f), which is similar to the Hubble-like velocity structure or Hubble flow. As described above, the ejected gas has different velocities and the gas with different velocities propagates along the z -axis. Thus, the highest-velocity gas is located farthest from the protostar as time proceeds. On the other hand, the low-velocity gas remains close to the protostar because their initial velocity (i.e., launching velocity) is low. As a result, the inclined spine-like structure appears in the PV diagram. In addition, the ejected gas interacts with the envelope material and thus decelerates. Therefore, a sharp spine widens with time and the propagation or jet velocity decelerates to have a velocity plateau, as seen in the right panels of Figure 8.

In Figure 8(f), we can see a new spine labeled as [3] in the PV diagram which corresponds to a new mass ejection event occurring at 201.69 yr after the protostar formation (Figure 8e). The spine inclines as time in the PV diagram. Reflecting the past mass ejection event, we can see, at least, three spike-like structures [1]-[3] in Figure 8(f). The spine gradually inclines and widens with time. In other words, the inclination angle and width of the spine at an old mass ejection event are more significant than that at a new mass ejection event.

Some morphological similarities between the observation (Figure 6) and simulation (Figure 8 left panels) are apparent. In addition, the PV diagrams made by the observation (Figure 5) and simulation (Figure 8) are qualitatively the same. However, the velocity distribution and the interval of the mass ejection events are not quantitatively the same between the observation and the simulation. Since the spatial resolution of the simulation is restricted, the timescale over which the PV diagram

varies is extremely short (months). We thus can not quantitatively compare the observation with the simulation.

Following the simulation, we interpret the observed PV diagram velocity distribution. Multiple mass ejection events produce the multiple spine-like structures seen in Figure 5. The different angles seen in the PV diagram can be explained by the time evolution of each jet component. The high-velocity gas component spreads fastest as the ejected gas moves away from the protostar. Thus, in the PV diagram the spine appears to incline with time. In addition, the interaction between the ejected gas and envelope material decelerates the jet and produces a velocity plateau. In Figure 5, for component [1] the farthest part of the spine reaches a constant velocity (i.e., velocity plateau), potential evidence for the decelerated gas. Such a velocity plateau has been reported in other protostellar systems (e.g., Wang et al. 2014; Matsushita et al. 2019; Morii et al. 2021b).

4.2. Jet Dynamical Model and Shock Chemistry

The PV diagram obtained from the simulation shows similar characteristics to those obtained from the SiO observation. However, the simulation PV diagram seems to differ from that found by previous outflow studies using CO, which mainly traces an older and static outflow, such as reported by Santiago-García et al. (2009) and Plunkett et al. (2015). Hence, we consider that the chemical processes in this extremely young jet are very active and may not be in a steady state. In this subsection, we discuss possible origins of the SiO emission observed toward MMS 1. We also discuss how they possibly relate to the mass ejection phenomena produced by the dynamical model presented in Subsection 4.1.

Three different paths are considered to release silicates into the gas phase and subsequently form the SiO molecules observed in jets (Cabrit et al. 2012; Podio et al. 2021). The first path is the sputtering of silicate grains in C-shocks, which requires a velocity differential in the range of 10 and 40 km s⁻¹ to produce SiO in the gas phase (e.g., Schilke et al. 1997; Caselli et al. 1997; Panoglou et al. 2012). The second path is the release of silicon into the gas phase by vaporization in grain-grain collisions, which is expected to occur in slow J-shocks ($\lesssim 50$ km s⁻¹) with the amount of silicon released into the gas phase on the order of a few percent (Guillet et al. 2009). The third path is the release of silicon into the gas phase in the region where the gas temperature reaches the dust sublimation temperature (Glassgold et al. 1991; Tabone et al. 2020).

The first case (C-shocks) has been discussed mainly for forming SiO in previously observed sources (Schilke

et al. 1997; Gusdorf et al. 2008a,b) for which SiO is known as a shock tracer. The second case (J-shocks) can be expected to occur in specific locations, such as at the apex of bow shocks (e.g., Hartigan et al. 2004). The PV-diagrams in the right panels of Figure 8 indicate that the jet velocity is consistent with that required to release the silicate grains into the gas phase either through the C- or J-shocks. Moreover, the numerical simulation performed by Machida et al. (2020) reveals that the region close to the jet driving region has density and temperature discontinuities, indicating the presence of J-shocks. These considerations imply that the observed SiO emission might be produced by both the first and second pathways above, C-shocks or J-shocks.

Regarding the third pathway, the launching point of the high-speed jet ($v_{\text{jet}} \sim 100$ km s⁻¹) is expected to be several $\times 0.1$ au (Figure 8 right panels). The temperature expected at these radii is a few $\times 1000$ K, assuming a source bolometric luminosity of $1 L_{\odot}$. This temperature is comparable to the dust sublimation temperature of 1500 K (e.g., Vaidya et al. 2009), implying that some of the observed high-velocity SiO components might be formed by this additional route.

Our gas-dynamic model (left panels of Figure 8) does not consider chemical networks. However, the physical conditions expected from this model are consistent with the conditions under which the SiO molecule could be formed, as predicted by the previous theoretical studies described above. Chemohydrodynamic analysis, where the chemical distribution is affected by the gas-dust dynamical evolution (e.g., Flower & Pineau des Forêts 2003; Godard et al. 2019; Castellanos-Ramírez et al. 2018), will be required to make complete comparisons in future studies.

4.3. Episodic Mass Ejection and Accretion

As discussed in Section 4.1, both observations and simulations clearly show evidence of the non-steady mass ejection events within protostellar jets. Recent ALMA CO and SiO observations toward protostellar sources reveal chains of knots within protostellar jets, suggesting episodic mass ejection events (Plunkett et al. 2015; Matsushita et al. 2019; Jhan et al. 2022; Dutta et al. 2022, 2023, and this work). The dynamical timescales between these ejection events range from several years to thousands of years. At the same time, recent flux variability surveys performed at sub-millimeter and mid-infrared wavelengths suggest that the fraction of variable sources is high during this protostellar phase (Johnstone et al. 2018; Lee et al. 2021; Park et al. 2021). Two distinct forms of variability are observed: years-long secular variability and short-timescale stochastic

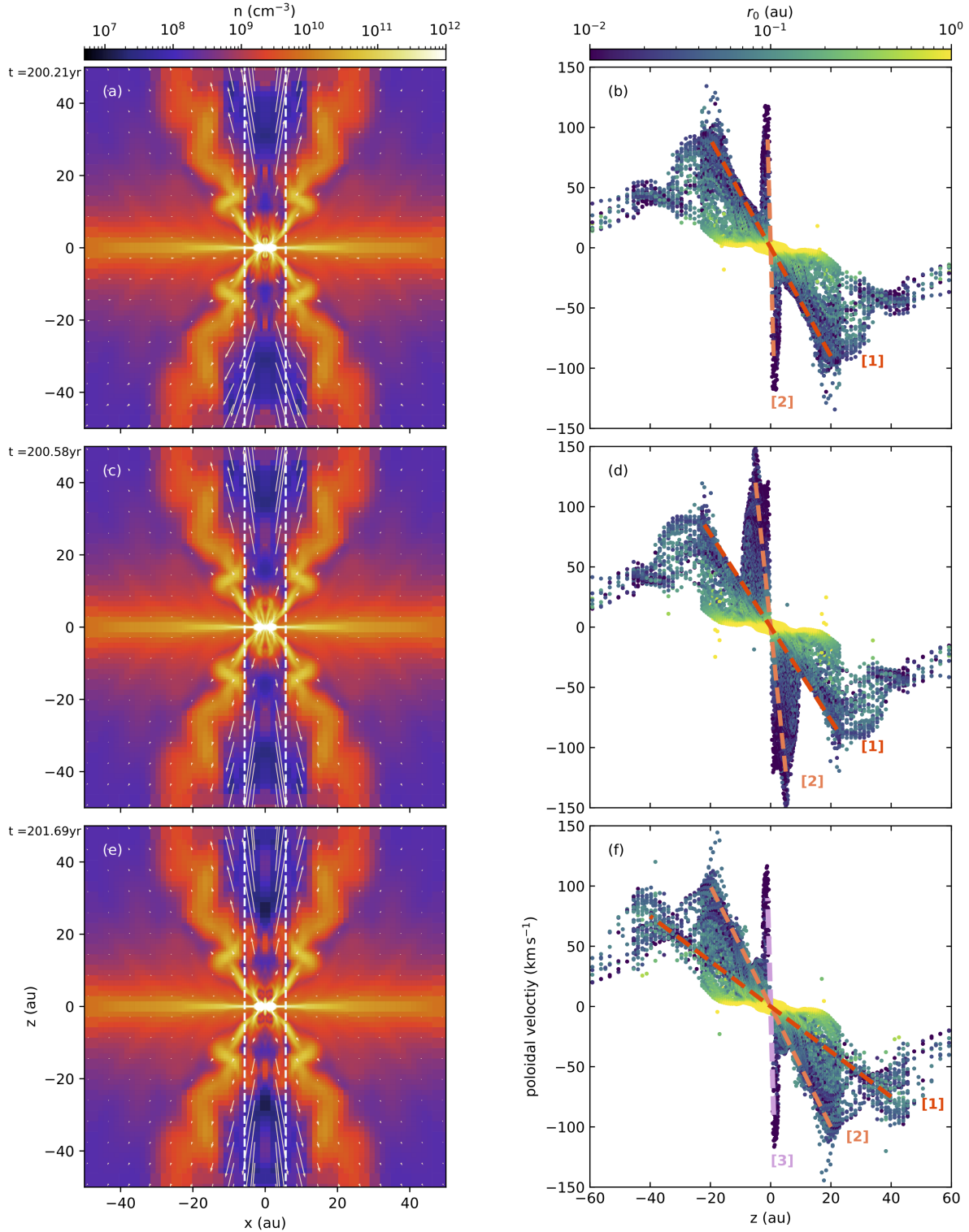


Figure 8. Time evolution of the density (color) and velocity (arrows) distributions (left panels) and the PV-diagram along the z -axis (right panels) made from the numerical simulations done by Machida & Basu (2019). The elapsed time after protostar formation t is described at the upper left corner of the left panels. In the right panels, the color within each circle corresponds to the jet launching radius calculated by the physical quantities derived from the simulation and analytical solutions in Anderson et al. (2003). The spine structures corresponding to the ejected clumps are labeled as [1], [2] and [3] in the right panels. For comparison with observational results (corresponding to labels [1], [2], and [3] in Figure 5), three recent ejection events are delineated by the orange dashed lines in the PV diagram of panel (f).

variability. The range of timescales is attributed to a variety of processes including underlying changes in the disk accretion rate, geometric changes in the circumstellar disk, hydromagnetic interactions between the stellar surface and inner disk, magnetic reconnection of the stellar magnetosphere, and the number or size of spots on the stellar surface (Park et al. 2021; Fischer et al. 2023). In conclusion, these monitoring studies demonstrate the importance of understanding the non-steady nature the star formation activities.

Figure 9 presents $850\ \mu\text{m}$ continuum flux monitoring results for MMS 1 obtained by the JCMT Transient Survey (Herczeg et al. 2017). The observations cover late 2015 through mid-2023, almost eight years of roughly monthly cadence. For bright sources, such as MMS 1, the relative flux calibration uncertainty between epochs is better than 2% (Mairs et al. 2017, Mairs et al. 2024 accepted by ApJ). No drastic flux change is detected from the $850\ \mu\text{m}$ light curve, suggesting that there has not been a clear burst event within the last 8 years. There is, however, a distinct $\sim 0.5\%$ per year gradual decline in the brightness - therefore a candidate linear variable, according to Mairs et al. (2024 accepted). The decline is similar, though shallower, to the observed decline in HOPS 383 (Lee et al. 2021), a protostar that had an observed mid-IR burst between 2004 and 2006 (Safron et al. 2015), about ten years prior to the start of the JCMT survey.

For MMS 1, the timescale of the episodic mass ejection events associated with the SiO knots presented in Figure 6 ranges from 5 to 50 years. Thus, the monitored time period might not be long enough to detect the associated episodic mass accretion phenomena. We note that $850\ \mu\text{m}$ burst events have been observed by the JCMT Transient Survey for a few protostars allowing for detailed consideration of the events. HOPS 373 underwent a months-long burst that was analysed by Yoon et al. (2022) and EC53 (also known as V371 Ser) has continuing quasi-periodic variations observed at both near-IR (Hodapp et al. 2012) and sub-mm (Yoo et al. 2017) leading to a multi-wavelength analysis by Lee et al. (2020) and an interferometric analysis by Francis et al. (2022). Thus far, however, neither of those two sources have had features in their outflow connected to the observed accretion bursts. Circumstantial evidence for accretion variability correlating with episodic mass ejection has been presented for a few Orion outflow sources through comparison of the ejection timescales and the observed accretion variability timescale found from mid-IR or sub-mm monitoring (Jhan et al. 2022; Dutta et al. 2023). Continued monitoring of MMS 1 at $850\ \mu\text{m}$, combined with proper motion measurements of

the SiO knots, will enable us to better determine the connection between episodic mass accretion events and episodic mass ejection.

Considering the current ALMA angular resolution of $\sim 0''.2$ and the observed maximum jet velocity of $\sim 70\ \text{km s}^{-1}$, our observations are only sensitive to the timescale longer than ~ 5 years. In order to detect less significant episodic events associated with a shorter time period than five years, higher angular resolution observations ($\lesssim 0''.2$) and mild shock tracers such as CH_3OH and H_2CO or S-bearing molecules might be useful (e.g., Lee et al. 2018; Tychoniec et al. 2019, 2021; Codella et al. 2020, 2021).

5. SUMMARY

We have performed CO (2–1), SiO (5–4), and 1.3 mm continuum observations using ALMA Band 6 toward an extremely young intermediate-mass protostellar source, MMS 1 located in the OMC-3 region.

1. We have detected bright compact 1.3 mm continuum emission. Assuming that the compact component fitted by the 2D Gaussian traces a dust disk, the size and mass of the dust disk are estimated to be ~ 33 au and $0.0051\text{--}0.020\ M_{\odot}$, respectively.
2. With the angular resolution of $\sim 0''.2$, we have detected the very compact molecular outflow in CO (2–1) and the jet in SiO (5–4) for the first time. The outflow and jet are aligned roughly perpendicular to the dust disk. The detected molecular outflow shows a cavity like structure with a wide opening angle. The SiO jet lies within the CO cavity. The jet length and velocity are calculated to be ~ 1300 au and $92\ \text{km s}^{-1}$ for the blue-shifted component, and 720 au and $62\ \text{km s}^{-1}$ for the red-shifted component after the correction for inclination. We confirm that the SiO jet wiggles. Within the jet knots are observed, which are particularly clear to the SW side of the jet.
3. The jet dynamical time scale is estimated to be 66 yr (blue-shifted component) and 55 yr (red-shifted component). These numbers indicate that the jet associated with MMS 1 is the youngest thus far reported. The dynamical timescale of each SiO knot with respect to the millimeter source peaks (i.e., protostar location) are estimated between 5 yr and 53 yr, possibly related to the timescale of episodic mass accretion events.
4. The PV-diagram cut along the SiO jet axis shows that the gas velocity linearly increases as the dis-

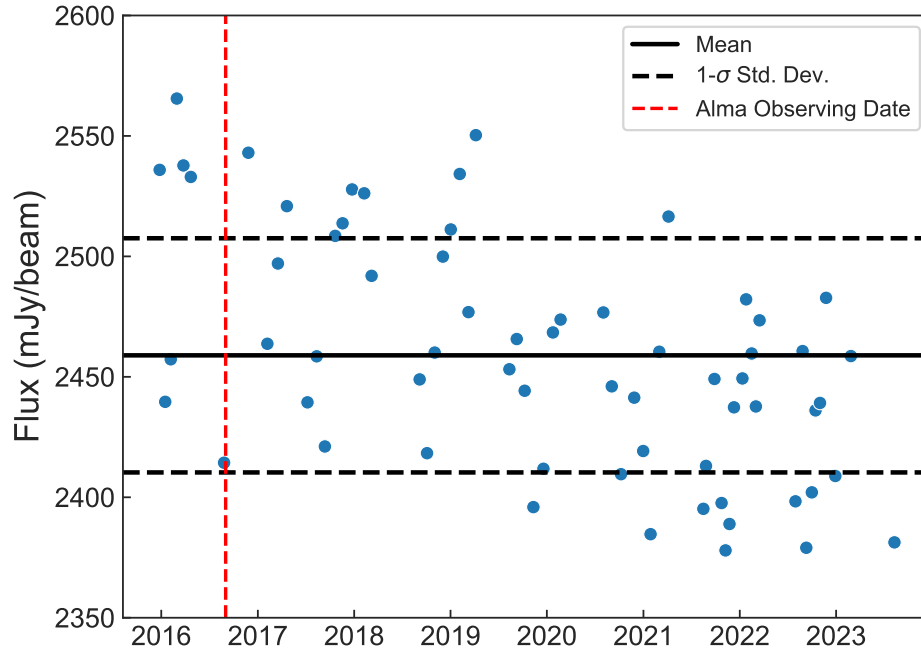


Figure 9. The $850\ \mu\text{m}$ light curve obtained with the JCMT/SCUBA2. The horizontal dashed lines give the uncertainties of $\pm 1\sigma$ due to calibration on individual measurements. The vertical red dashed line shows the date at which the high-angular resolution ALMA observation, presented in this paper was performed.

tance from the protostar increases (a.k.a. Hubble-like velocity structure). The SiO emission associated with each knot shows a different inclination angle (or slope) in the PV-diagram. A numerical simulation of core collapse by Machida & Basu (2019) can qualitatively reproduce similar features in the PV-diagram. The comparison suggests that the observed SiO jet may be explained by multiple-mass ejection events, which produce the multiple-spine-like structure observed in the PV-diagram.

- Finally, the $850\ \mu\text{m}$ light curve obtained with the JCMT/SCUBA 2 toward MMS1 is presented. The plot indicates no significant time variability, such as large burst or drop, over the last eight years. A weak decrease in the flux with time might be related to changes in the mass accretion rate, similar to that observed for HOPS 383. Continued sub-mm flux monitoring combined with proper motion measurements of the jet knots may reveal how episodic mass ejection events are connected to the episodic mass accretion history of MMS1.

Acknowledgements.

We thank the anonymous referee for providing very helpful comments and useful suggestions, which improve the manuscript significantly. This paper makes use of the following ALMA data: ADS/JAO.ALMA#2015.1.00341.S. ALMA is a partnership of ESO (representing its member states), NSF (USA) and NINS (Japan), together with NRC (Canada), MOST and ASIAA (Taiwan), and KASI (Republic of Korea), in cooperation with the Republic of Chile. The Joint ALMA Observatory is operated by ESO, AUI/NRAO and NAOJ. Data analysis was carried out on the Multi-wavelength Data Analysis System operated by the Astronomy Data Center (ADC), National Astronomical Observatory of Japan. We acknowledge the JCMT transient team providing us the eight years light curve obtained in the $850\ \mu\text{m}$ continuum emission using SCUBA 2, which was used to compare with our ALMA data set in Figure 9. This work was supported by JSPS KAKENHI Grant Number JP19K03919(KT), and JP21K03617 and JP21H0046 (MNM). L.A.Z. acknowledges financial support from CONACyT-280775 and UNAM-PAPIIT IN110618, and IN112323 grants, México. D.J. is supported by NRC Canada and by an NSERC Discovery Grant.

*Facilities:*ALMA; JCMT

REFERENCES

- Anderson, J. M., Li, Z.-Y., Krasnopolsky, R., & Blandford, R. D. 2003, *ApJL*, 590, L107, doi: [10.1086/376824](https://doi.org/10.1086/376824)
- Arce, H. G., Shepherd, D., Gueth, F., et al. 2007, in *Protostars and Planets V*, ed. B. Reipurth, D. Jewitt, & K. Keil, 245. <https://arxiv.org/abs/astro-ph/0603071>
- Aso, Y., Tatematsu, K., Sekimoto, Y., et al. 2000, *ApJS*, 131, 465, doi: [10.1086/317378](https://doi.org/10.1086/317378)
- Bachiller, R. 1996, *A&A*, 34, 111, doi: [10.1146/annurev.astro.34.1.111](https://doi.org/10.1146/annurev.astro.34.1.111)
- Bachiller, R., & Cernicharo, J. 1990, *A&A*, 239, 276
- Bachiller, R., Gueth, F., Guilloteau, S., Tafalla, M., & Dutrey, A. 2000, *A&A*, 362, L33. <https://arxiv.org/abs/astro-ph/0009439>
- Bachiller, R., Martin-Pintado, J., & Fuente, A. 1991a, *A&A*, 243, L21
- Bachiller, R., Martin-Pintado, J., & Planesas, P. 1991b, *A&A*, 251, 639
- Bachiller, R., & Tafalla, M. 1999, in *NATO Advanced Science Institutes (ASI) Series C*, Vol. 540, NATO Advanced Science Institutes (ASI) Series C, ed. C. J. Lada & N. D. Kylafis, 227
- Bally, J. 2016, *ARA&A*, 54, 491, doi: [10.1146/annurev-astro-081915-023341](https://doi.org/10.1146/annurev-astro-081915-023341)
- Bjerkeli, P., van der Wiel, M. H. D., Harsono, D., Ramsey, J. P., & Jørgensen, J. K. 2016, *Nature*, 540, 406, doi: [10.1038/nature20600](https://doi.org/10.1038/nature20600)
- Blandford, R. D., & Payne, D. G. 1982, *MNRAS*, 199, 883, doi: [10.1093/mnras/199.4.883](https://doi.org/10.1093/mnras/199.4.883)
- Cabrit, S., Codella, C., Gueth, F., & Gusdorf, A. 2012, *A&A*, 548, L2, doi: [10.1051/0004-6361/201219784](https://doi.org/10.1051/0004-6361/201219784)
- CASA team, Bean, B., Bhatnagar, S., et al. 2022, arXiv e-prints, arXiv:2210.02276. <https://arxiv.org/abs/2210.02276>
- Caselli, P., Hartquist, T. W., & Havnes, O. 1997, *A&A*, 322, 296
- Castellanos-Ramírez, A., Raga, A. C., & Rodríguez-González, A. 2018, *ApJ*, 867, 29, doi: [10.3847/1538-4357/aae088](https://doi.org/10.3847/1538-4357/aae088)
- Chini, R., Reipurth, B., Ward-Thompson, D., et al. 1997, *ApJL*, 474, L135, doi: [10.1086/310436](https://doi.org/10.1086/310436)
- Codella, C., Ceccarelli, C., Bianchi, E., et al. 2020, *A&A*, 635, A17, doi: [10.1051/0004-6361/201936725](https://doi.org/10.1051/0004-6361/201936725)
- Codella, C., Bianchi, E., Podio, L., et al. 2021, *A&A*, 654, A52, doi: [10.1051/0004-6361/202141485](https://doi.org/10.1051/0004-6361/202141485)
- de A. Schutzer, A., Rivera-Ortiz, P. R., Lefloch, B., et al. 2022, *A&A*, 662, A104, doi: [10.1051/0004-6361/202142931](https://doi.org/10.1051/0004-6361/202142931)
- Dutta, S., Lee, C.-F., Hirano, N., et al. 2022, *ApJ*, 931, 130, doi: [10.3847/1538-4357/ac67a1](https://doi.org/10.3847/1538-4357/ac67a1)
- Dutta, S., Lee, C.-F., Johnstone, D., et al. 2023, arXiv e-prints, arXiv:2306.15346, doi: [10.48550/arXiv.2306.15346](https://doi.org/10.48550/arXiv.2306.15346)
- Fischer, W. J., Hillenbrand, L. A., Herczeg, G. J., et al. 2023, in *Astronomical Society of the Pacific Conference Series*, Vol. 534, *Protostars and Planets VII*, ed. S. Inutsuka, Y. Aikawa, T. Muto, K. Tomida, & M. Tamura, 355, doi: [10.48550/arXiv.2203.11257](https://doi.org/10.48550/arXiv.2203.11257)
- Flower, D. R., & Pineau des Forêts, G. 2003, *MNRAS*, 343, 390, doi: [10.1046/j.1365-8711.2003.06716.x](https://doi.org/10.1046/j.1365-8711.2003.06716.x)
- Francis, L., Johnstone, D., Lee, J.-E., et al. 2022, *ApJ*, 937, 29, doi: [10.3847/1538-4357/ac8a9e](https://doi.org/10.3847/1538-4357/ac8a9e)
- Frank, A., Ray, T. P., Cabrit, S., et al. 2014, in *Protostars and Planets VI*, ed. H. Beuther, R. S. Klessen, C. P. Dullemond, & T. Henning, 451–474, doi: [10.2458/azu_uapress.9780816531240-ch020](https://doi.org/10.2458/azu_uapress.9780816531240-ch020)
- Furlan, E., Fischer, W. J., Ali, B., et al. 2016, *ApJS*, 224, 5, doi: [10.3847/0067-0049/224/1/5](https://doi.org/10.3847/0067-0049/224/1/5)
- Gaia Collaboration, Brown, A. G. A., Vallenari, A., et al. 2018, *A&A*, 616, A1, doi: [10.1051/0004-6361/201833051](https://doi.org/10.1051/0004-6361/201833051)
- Gerin, M., Pety, J., Fuente, A., et al. 2015, *A&A*, 577, L2, doi: [10.1051/0004-6361/201525777](https://doi.org/10.1051/0004-6361/201525777)
- Glassgold, A. E., Mamon, G. A., & Huggins, P. J. 1991, *ApJ*, 373, 254, doi: [10.1086/170045](https://doi.org/10.1086/170045)
- Godard, B., Pineau des Forêts, G., Lesaffre, P., et al. 2019, *A&A*, 622, A100, doi: [10.1051/0004-6361/201834248](https://doi.org/10.1051/0004-6361/201834248)
- Gómez-Ruiz, A. I., Gusdorf, A., Leurini, S., et al. 2019, *A&A*, 629, A77, doi: [10.1051/0004-6361/201424156](https://doi.org/10.1051/0004-6361/201424156)
- Gómez-Ruiz, A. I., Hirano, N., Leurini, S., & Liu, S. Y. 2013, *A&A*, 558, A94, doi: [10.1051/0004-6361/201118473](https://doi.org/10.1051/0004-6361/201118473)
- Guillet, V., Jones, A. P., & Pineau Des Forêts, G. 2009, *A&A*, 497, 145, doi: [10.1051/0004-6361/200811115](https://doi.org/10.1051/0004-6361/200811115)
- Gusdorf, A., Cabrit, S., Flower, D. R., & Pineau Des Forêts, G. 2008a, *A&A*, 482, 809, doi: [10.1051/0004-6361:20078900](https://doi.org/10.1051/0004-6361:20078900)
- Gusdorf, A., Pineau Des Forêts, G., Cabrit, S., & Flower, D. R. 2008b, *A&A*, 490, 695, doi: [10.1051/0004-6361:200810443](https://doi.org/10.1051/0004-6361:200810443)
- Hartigan, P., Raymond, J., & Pierson, R. 2004, *ApJL*, 614, L69, doi: [10.1086/425322](https://doi.org/10.1086/425322)
- Herczeg, G. J., Johnstone, D., Mairs, S., et al. 2017, *ApJ*, 849, 43, doi: [10.3847/1538-4357/aa8b62](https://doi.org/10.3847/1538-4357/aa8b62)
- Hirano, N., Ho, P. P. T., Liu, S.-Y., et al. 2010, *ApJ*, 717, 58, doi: [10.1088/0004-637X/717/1/58](https://doi.org/10.1088/0004-637X/717/1/58)
- Hirano, N., & Liu, F.-c. 2014, *ApJ*, 789, 50, doi: [10.1088/0004-637X/789/1/50](https://doi.org/10.1088/0004-637X/789/1/50)
- Hirano, S., & Machida, M. N. 2019, *MNRAS*, 485, 4667, doi: [10.1093/mnras/stz740](https://doi.org/10.1093/mnras/stz740)

- Hirano, S., Tsukamoto, Y., Basu, S., & Machida, M. N. 2020, *ApJ*, 898, 118, doi: [10.3847/1538-4357/ab9f9d](https://doi.org/10.3847/1538-4357/ab9f9d)
- Hirota, T., Bushimata, T., Choi, Y. K., et al. 2007, *PASJ*, 59, 897, doi: [10.1093/pasj/59.5.897](https://doi.org/10.1093/pasj/59.5.897)
- Hodapp, K. W., Chini, R., Watermann, R., & Lemke, R. 2012, *ApJ*, 744, 56, doi: [10.1088/0004-637X/744/1/56](https://doi.org/10.1088/0004-637X/744/1/56)
- Jhan, K.-S., Lee, C.-F., Johnstone, D., et al. 2022, *ApJL*, 931, L5, doi: [10.3847/2041-8213/ac6a53](https://doi.org/10.3847/2041-8213/ac6a53)
- Johnstone, D., & Bally, J. 1999, *ApJL*, 510, L49, doi: [10.1086/311792](https://doi.org/10.1086/311792)
- Johnstone, D., Herczeg, G. J., Mairs, S., et al. 2018, *ApJ*, 854, 31, doi: [10.3847/1538-4357/aaa764](https://doi.org/10.3847/1538-4357/aaa764)
- Jørgensen, J. K., Visser, R., Sakai, N., et al. 2013, *ApJL*, 779, L22, doi: [10.1088/2041-8205/779/2/L22](https://doi.org/10.1088/2041-8205/779/2/L22)
- Kim, M. K., Hirota, T., Honma, M., et al. 2008, *PASJ*, 60, 991, doi: [10.1093/pasj/60.5.991](https://doi.org/10.1093/pasj/60.5.991)
- Kounkel, M., Hartmann, L., Loinard, L., et al. 2017, *ApJ*, 834, 142, doi: [10.3847/1538-4357/834/2/142](https://doi.org/10.3847/1538-4357/834/2/142)
- Kounkel, M., Covey, K., Suárez, G., et al. 2018, *AJ*, 156, 84, doi: [10.3847/1538-3881/aad1f1](https://doi.org/10.3847/1538-3881/aad1f1)
- Larson, R. B. 1969, *MNRAS*, 145, 271, doi: [10.1093/mnras/145.3.271](https://doi.org/10.1093/mnras/145.3.271)
- Lebrón, M., Beuther, H., Schilke, P., & Stanke, T. 2006, *A&A*, 448, 1037, doi: [10.1051/0004-6361:20041852](https://doi.org/10.1051/0004-6361:20041852)
- Lee, C.-F. 2020, *A&A Rv*, 28, 1, doi: [10.1007/s00159-020-0123-7](https://doi.org/10.1007/s00159-020-0123-7)
- Lee, C.-F., Ho, P. T. P., Li, Z.-Y., et al. 2017, *Nature Astronomy*, 1, 0152, doi: [10.1038/s41550-017-0152](https://doi.org/10.1038/s41550-017-0152)
- Lee, C.-F., Li, Z.-Y., Hirano, N., et al. 2018, *ApJ*, 863, 94, doi: [10.3847/1538-4357/aad2da](https://doi.org/10.3847/1538-4357/aad2da)
- Lee, Y.-H., Johnstone, D., Lee, J.-E., et al. 2020, *ApJ*, 903, 5, doi: [10.3847/1538-4357/abb6fe](https://doi.org/10.3847/1538-4357/abb6fe)
- . 2021, *ApJ*, 920, 119, doi: [10.3847/1538-4357/ac1679](https://doi.org/10.3847/1538-4357/ac1679)
- Lis, D. C., Serabyn, E., Keene, J., et al. 1998, *ApJ*, 509, 299, doi: [10.1086/306500](https://doi.org/10.1086/306500)
- Liu, Y., Takahashi, S., Machida, M., et al. 2023, arXiv e-prints, arXiv:2312.13573, doi: [10.48550/arXiv.2312.13573](https://doi.org/10.48550/arXiv.2312.13573)
- Lynden-Bell, D. 2003, *MNRAS*, 341, 1360, doi: [10.1046/j.1365-8711.2003.06506.x](https://doi.org/10.1046/j.1365-8711.2003.06506.x)
- Machida, M. N. 2014, *ApJL*, 796, L17, doi: [10.1088/2041-8205/796/1/L17](https://doi.org/10.1088/2041-8205/796/1/L17)
- Machida, M. N., & Basu, S. 2019, *ApJ*, 876, 149, doi: [10.3847/1538-4357/ab18a7](https://doi.org/10.3847/1538-4357/ab18a7)
- Machida, M. N., Hirano, S., & Kitta, H. 2020, *MNRAS*, 491, 2180, doi: [10.1093/mnras/stz3159](https://doi.org/10.1093/mnras/stz3159)
- Machida, M. N., & Hosokawa, T. 2013, *MNRAS*, 431, 1719, doi: [10.1093/mnras/stt291](https://doi.org/10.1093/mnras/stt291)
- Machida, M. N., Inutsuka, S., & Matsumoto, T. 2007, *ApJ*, 670, 1198, doi: [10.1111/j.1365-2966.2011.20336.x](https://doi.org/10.1111/j.1365-2966.2011.20336.x)
- Machida, M. N., Tomisaka, K., & Matsumoto, T. 2004, *MNRAS*, 348, L1, doi: [10.1111/j.1365-2966.2004.07402.x](https://doi.org/10.1111/j.1365-2966.2004.07402.x)
- Mairs, S., Lane, J., Johnstone, D., et al. 2017, *ApJ*, 843, 55, doi: [10.3847/1538-4357/aa7844](https://doi.org/10.3847/1538-4357/aa7844)
- Masciadri, E., & Raga, A. C. 2002, *ApJ*, 568, 733, doi: [10.1086/338767](https://doi.org/10.1086/338767)
- Masunaga, H., & Inutsuka, S. 2000, *ApJ*, 531, 350, doi: [10.1086/308439](https://doi.org/10.1086/308439)
- Mathis, J. S., Rumpl, W., & Nordsieck, K. H. 1977, *ApJ*, 217, 425, doi: [10.1086/155591](https://doi.org/10.1086/155591)
- Matsushita, Y., Takahashi, S., Machida, M. N., & Tomisaka, K. 2019, *ApJ*, 871, 221, doi: [10.3847/1538-4357/aaf1b6](https://doi.org/10.3847/1538-4357/aaf1b6)
- Maureira, M. J., Arce, H. G., Dunham, M. M., et al. 2020, *MNRAS*, 499, 4394, doi: [10.1093/mnras/staa2894](https://doi.org/10.1093/mnras/staa2894)
- McBride, A., & Kounkel, M. 2019, *ApJ*, 884, 6, doi: [10.3847/1538-4357/ab3df9](https://doi.org/10.3847/1538-4357/ab3df9)
- Megeath, S. T., Gutermuth, R., Muzerolle, J., et al. 2012, *AJ*, 144, 192, doi: [10.1088/0004-6256/144/6/192](https://doi.org/10.1088/0004-6256/144/6/192)
- Menten, K. M., Reid, M. J., Forbrich, J., & Brunthaler, A. 2007, *A&A*, 474, 515, doi: [10.1051/0004-6361:20078247](https://doi.org/10.1051/0004-6361:20078247)
- Morii, K., Takahashi, S., & Machida, M. N. 2021a, *ApJ*, 910, 148, doi: [10.3847/1538-4357/abe61c](https://doi.org/10.3847/1538-4357/abe61c)
- Morii, K., Sanhueza, P., Nakamura, F., et al. 2021b, *ApJ*, 923, 147, doi: [10.3847/1538-4357/ac2365](https://doi.org/10.3847/1538-4357/ac2365)
- Nomura, H., & Millar, T. J. 2005, *A&A*, 438, 923, doi: [10.1051/0004-6361:20052809](https://doi.org/10.1051/0004-6361:20052809)
- Ossenkopf, V., & Henning, T. 1994, *A&A*, 291, 943
- Panoglou, D., Cabrit, S., Pineau Des Forêts, G., et al. 2012, *A&A*, 538, A2, doi: [10.1051/0004-6361/200912861](https://doi.org/10.1051/0004-6361/200912861)
- Park, W., Lee, J.-E., Contreras Peña, C., et al. 2021, *ApJ*, 920, 132, doi: [10.3847/1538-4357/ac1745](https://doi.org/10.3847/1538-4357/ac1745)
- Plunkett, A. L., Arce, H. G., Mardones, D., et al. 2015, *Nature*, 527, 70, doi: [10.1038/nature15702](https://doi.org/10.1038/nature15702)
- Podio, L., Tabone, B., Codella, C., et al. 2021, *A&A*, 648, A45, doi: [10.1051/0004-6361/202038429](https://doi.org/10.1051/0004-6361/202038429)
- Raga, A. C., Canto, J., & Biro, S. 1993, *MNRAS*, 260, 163, doi: [10.1093/mnras/260.1.163](https://doi.org/10.1093/mnras/260.1.163)
- Reipurth, B., Rodríguez, L. F., & Chini, R. 1999, *AJ*, 118, 983, doi: [10.1086/300958](https://doi.org/10.1086/300958)
- Safron, E. J., Fischer, W. J., Megeath, S. T., et al. 2015, *ApJL*, 800, L5, doi: [10.1088/2041-8205/800/1/L5](https://doi.org/10.1088/2041-8205/800/1/L5)
- Saigo, K., & Tomisaka, K. 2006, *ApJ*, 645, 381, doi: [10.1086/504028](https://doi.org/10.1086/504028)
- Sandstrom, K. M., Peek, J. E. G., Bower, G. C., Bolatto, A. D., & Plambeck, R. L. 2007, *ApJ*, 667, 1161, doi: [10.1086/520922](https://doi.org/10.1086/520922)

- Santiago-García, J., Tafalla, M., Johnstone, D., & Bachiller, R. 2009, *A&A*, 495, 169, doi: [10.1051/0004-6361:200810739](https://doi.org/10.1051/0004-6361:200810739)
- Schilke, P., Walmsley, C. M., Pineau des Forets, G., & Flower, D. R. 1997, *A&A*, 321, 293
- Shang, H., Liu, C.-F., Krasnopolsky, R., & Wang, L.-Y. 2023, *ApJ*, 944, 230, doi: [10.3847/1538-4357/aca763](https://doi.org/10.3847/1538-4357/aca763)
- Sharma, R., Tobin, J. J., Sheehan, P. D., et al. 2020, *ApJ*, 904, 78, doi: [10.3847/1538-4357/abdbf4](https://doi.org/10.3847/1538-4357/abdbf4)
- Shu, F., Najita, J., Ostriker, E., et al. 1994, *ApJ*, 429, 781, doi: [10.1086/174363](https://doi.org/10.1086/174363)
- Stanke, T., McCaughrean, M. J., & Zinnecker, H. 2002, *A&A*, 392, 239, doi: [10.1051/0004-6361:20020763](https://doi.org/10.1051/0004-6361:20020763)
- Stutz, A. M., Tobin, J. J., Stanke, T., et al. 2013, *ApJ*, 767, 36, doi: [10.1088/0004-637X/767/1/36](https://doi.org/10.1088/0004-637X/767/1/36)
- Tabone, B., Cabrit, S., Pineau des Forêts, G., et al. 2020, *A&A*, 640, A82, doi: [10.1051/0004-6361/201834377](https://doi.org/10.1051/0004-6361/201834377)
- Tafalla, M., Su, Y. N., Shang, H., et al. 2017, *A&A*, 597, A119, doi: [10.1051/0004-6361/201629493](https://doi.org/10.1051/0004-6361/201629493)
- Takahashi, S., & Ho, P. T. P. 2012, *ApJL*, 745, L10, doi: [10.1088/2041-8205/745/1/L10](https://doi.org/10.1088/2041-8205/745/1/L10)
- Takahashi, S., Ho, P. T. P., Tang, Y.-W., Kawabe, R., & Saito, M. 2009, *ApJ*, 704, 1459, doi: [10.1088/0004-637X/704/2/1459](https://doi.org/10.1088/0004-637X/704/2/1459)
- Takahashi, S., Ho, P. T. P., Teixeira, P. S., Zapata, L. A., & Su, Y.-N. 2013a, *ApJ*, 763, 57, doi: [10.1088/0004-637X/763/1/57](https://doi.org/10.1088/0004-637X/763/1/57)
- Takahashi, S., Machida, M. N., Tomisaka, K., et al. 2019, *ApJ*, 872, 70, doi: [10.3847/1538-4357/aaf6ed](https://doi.org/10.3847/1538-4357/aaf6ed)
- Takahashi, S., Ohashi, N., & Bourke, T. L. 2013b, *ApJ*, 774, 20, doi: [10.1088/0004-637X/774/1/20](https://doi.org/10.1088/0004-637X/774/1/20)
- Takahashi, S., Saigo, K., Ho, P. T. P., & Tomida, K. 2012, *ApJ*, 752, 10, doi: [10.1088/0004-637X/752/1/10](https://doi.org/10.1088/0004-637X/752/1/10)
- Takahashi, S., Saigo, K., Ho, P. T. P., & Tomida, K. 2012, *ApJ*, 752, 10, doi: [10.1088/0004-637x/752/1/10](https://doi.org/10.1088/0004-637x/752/1/10)
- Takahashi, S., Saito, M., Ohashi, N., et al. 2008, *ApJ*, 688, 344, doi: [10.1086/592212](https://doi.org/10.1086/592212)
- Takahashi, S., Saito, M., Takakuwa, S., & Kawabe, R. 2006, *ApJ*, 651, 933, doi: [10.1086/507482](https://doi.org/10.1086/507482)
- Takami, M., Beck, T. L., Schneider, P. C., et al. 2020, *ApJ*, 901, 24, doi: [10.3847/1538-4357/abab98](https://doi.org/10.3847/1538-4357/abab98)
- Takami, M., Günther, H. M., Schneider, P. C., et al. 2023, *ApJS*, 264, 1, doi: [10.3847/1538-4365/ac9afc](https://doi.org/10.3847/1538-4365/ac9afc)
- Terquem, C., Eislöffel, J., Papaloizou, J. C. B., & Nelson, R. P. 1999, *ApJL*, 512, L131, doi: [10.1086/311880](https://doi.org/10.1086/311880)
- Tobin, J. J., Sheehan, P. D., Megeath, S. T., et al. 2020, *ApJ*, 890, 130, doi: [10.3847/1538-4357/ab6f64](https://doi.org/10.3847/1538-4357/ab6f64)
- Tokuda, K., Fujishiro, K., Tachihara, K., et al. 2020, *ApJ*, 899, 10, doi: [10.3847/1538-4357/ab9ca7](https://doi.org/10.3847/1538-4357/ab9ca7)
- Tomida, K., Machida, M. N., Hosokawa, T., Sakurai, Y., & Lin, C. H. 2017, *ApJL*, 835, L11, doi: [10.3847/2041-8213/835/1/L11](https://doi.org/10.3847/2041-8213/835/1/L11)
- Tomisaka, K. 2002, *ApJ*, 575, 306, doi: [10.1086/341133](https://doi.org/10.1086/341133)
- Tychoniec, L., Hull, C. L. H., Kristensen, L. E., et al. 2019, *A&A*, 632, A101, doi: [10.1051/0004-6361/201935409](https://doi.org/10.1051/0004-6361/201935409)
- Tychoniec, L., van Dishoeck, E. F., van't Hoff, M. L. R., et al. 2021, *A&A*, 655, A65, doi: [10.1051/0004-6361/202140692](https://doi.org/10.1051/0004-6361/202140692)
- Uchida, Y., & Shibata, K. 1985, *PASJ*, 37, 515
- Vaidya, B., Fendt, C., & Beuther, H. 2009, *ApJ*, 702, 567, doi: [10.1088/0004-637X/702/1/567](https://doi.org/10.1088/0004-637X/702/1/567)
- Wang, L.-Y., Shang, H., Su, Y.-N., et al. 2014, *ApJ*, 780, 49, doi: [10.1088/0004-637X/780/1/49](https://doi.org/10.1088/0004-637X/780/1/49)
- Williams, J. P., Plambeck, R. L., & Heyer, M. H. 2003, *ApJ*, 591, 1025, doi: [10.1086/375396](https://doi.org/10.1086/375396)
- Xu, W., & Kunz, M. W. 2021, *MNRAS*, 508, 2142, doi: [10.1093/mnras/stab2715](https://doi.org/10.1093/mnras/stab2715)
- Yoo, H., Lee, J.-E., Mairs, S., et al. 2017, *ApJ*, 849, 69, doi: [10.3847/1538-4357/aa8c0a](https://doi.org/10.3847/1538-4357/aa8c0a)
- Yoon, S.-Y., Herczeg, G. J., Lee, J.-E., et al. 2022, *ApJ*, 929, 60, doi: [10.3847/1538-4357/ac5632](https://doi.org/10.3847/1538-4357/ac5632)
- Yu, K. C., Bally, J., & Devine, D. 1997, *ApJL*, 485, L45, doi: [10.1086/310799](https://doi.org/10.1086/310799)
- Zakri, W., Megeath, S. T., Fischer, W. J., et al. 2022, *ApJL*, 924, L23, doi: [10.3847/2041-8213/ac46ae](https://doi.org/10.3847/2041-8213/ac46ae)
- Zapata, L. A., Rodríguez, L. F., Ho, P. T. P., et al. 2005, *ApJL*, 630, L85, doi: [10.1086/491470](https://doi.org/10.1086/491470)
- Zapata, L. A., Galván-Madrid, R., Carrasco-González, C., et al. 2015, *ApJL*, 811, L4, doi: [10.1088/2041-8205/811/1/L4](https://doi.org/10.1088/2041-8205/811/1/L4)